

## **ABSTRACT**

Title of Thesis: DESIGN AND ANALYSIS OF A MULTI-SECTION  
VARIABLE CAMBER WING

Prasobchok Poonsong, Master of Science, 2004

Thesis Directed by: Associate Professor Darryll Pines  
Department of Aerospace Engineering

Minimizing fuel consumption is one of the major concerns in the aviation industry. In the past decade, there have been many attempts to improve the fuel efficiency of aircraft. One of the methods proposed is to vary the lift-to-drag ratio of the aircraft in different flight conditions. To achieve this, the wing of the airplane must be able to change its configuration during flight, corresponding to different flight regimes.

In the research presented in this thesis, the aerodynamic characteristics of a multi-section, variable camber wing were investigated. The model used in this research had a 1-ft chord and a 1-ft wingspan, with the ribs divided into 6 sections. Each section was able to rotate approximately 5 degrees without causing significant discontinuity on the wing surface. Two pneumatic actuators located at the main spar were used to morph the wing through mechanical linkages. The multi-section variable camber wing model could provide up to 10 percent change in camber from the baseline configuration, which had a NACA0012 section.

The wing was tested in the free-jet wind tunnel at three different Reynolds numbers: 322000, 48000, and 636000. Static tests were performed to obtain lift and drag data for different configurations. Two rigid wings in baseline and camber configuration were built and tested to compare the test data with variable camber wing. The wind tunnel test results indicated that the multi-section variable camber wing provided a higher lift than the rigid wing in both configurations whereas high drag was also generated on the variable camber wing due to friction drag on the wing skin. The larger drag value appeared on variable camber wing in baseline configuration than in cambered configuration resulting in lower lift-to-drag ratio as compared to the baseline rigid wing whereas the variable camber wing in cambered configuration had higher lift-to-drag ratio than the cambered rigid wing.

DESIGN AND ANALYSIS OF MULTI-SECTION VARIABLE CAMBER WING

by

Prasobchok Poonsong

Thesis submitted to the Faculty of the Graduate School of the  
University of Maryland, College Park in partial fulfillment  
of the requirements for the degree of  
Master of Science  
2004

Advisory Committee:

Associate Professor Darryll Pines, Chair/Advisor

Associate Professor Allen Winkelmann

Associate Professor Alison Flatau



## ACKNOWLEDGEMENT

I would like to thank the Department of Aerospace Engineering of the University of Maryland for offering me an opportunity to bring my engineering skills to a higher level.

Thank you to Dr. Pines for getting me into this program, without you, I might have been serving in the Thai Air Force for the past two years and may have never had the chance to come back for graduate school. It was such a excellent opportunity for me. You are a great advisor, thank you for understanding the circumstances surrounding my situation.

Thank you to Dr. Winkelmann and Dr. Flatau for serving in my committee.

Thank you to Bernie, Les, and Charles at the wind tunnel for helping me make parts and allowing me to use the machines to make my wing.

Thank you to Dr. Winkelmann for your assistance and letting me use the free-jet wind tunnel and other equipment relating to wind tunnel testing.

Thank you to Matt Fox and Core Lab for allowing me to use the facility to make my wing.

Thank you to Ramy for helping me with a lot of things. You were there to help me cut the foam and run the tests until 5:00 in the morning. You are such a great friend.

Thank you to Jason Pereira, Nick Rosenfelt, and Paul, Julie, Ashish, Sandra, Felipe, and Gong Wang for correcting my paper and presentation.

Thank you to all the staff in the main office, especially, Julia John, you are very sweet.

Thank you to Emily for being there for me, you are a great support!

Last I have to thank everybody in my family; my mother, my father and especially my grandmother, even though you were in Thailand, I could feel your presence beside me the entire time.

## TABLE OF CONTENTS

LIST OF TABLES	vi
LIST OF FIGURES	vii
LIST OF ABBREVIATIONS	xi
NOMENCLATURE	xii
<b>1 INTRODUCTION</b>	<b>1</b>
1.1 MOTIVATION	2
1.2 OBJECTIVE	4
1.3 OUTLINE	5
1.4 TECHNICAL CHALLENGES	6
1.5 THESIS CONTENTS	8
<b>2 OVERVIEW OF VARIABLE CAMBER WING</b>	<b>9</b>
2.1 VARIABLE CAMBER WING IN THE PAST	9
2.2 CONTEMPORARY VARIABLE WING AND CONCEPTS	13
2.2.1 <i>High-Lift Devices</i>	13
2.2.2 <i>Mission Adaptive Wing (MAV)</i>	16
2.2.3 <i>Active Aeroelastic Wing (AAW)</i>	18
2.2.4 <i>Variform Wing Concept and Buckle-Wing Biplane</i>	19
2.3 SMART MATERIALS AND VARIABLE CAMBER WING	21
2.3.1 <i>Compliant Mechanism</i>	22
2.3.2 <i>Piezoelectric Actuator and Variable Camber Wing</i>	23
2.3.3 <i>Reconfigurable Wing</i>	26
2.3.4 <i>DARPA/Wright Lab “Smart Wing”</i>	27
<b>3 VARIABLE CAMBER WING DESIGN</b>	<b>30</b>
3.1 INITIAL CONCEPT	30
3.2 MULTI-SECTION VARIABLE CAMBER WING	31
3.2.1 <i>Wing Ribs and Spars</i>	31
3.2.2 <i>Actuators</i>	33
3.2.3 <i>Wing Structures Assembly</i>	37
3.2.4 <i>Wing Skin</i>	41
3.3 RIGID WING MODELS	42

<b>4</b>	<b>AERODYNAMIC ANALYSIS</b>	<b>44</b>
4.1	AIRCRAFT RANGE AND ENDURANCE	44
4.2	DEVELOPMENT OF THE ESTIMATED LIFT AND DRAG	47
	4.2.1 <i>Lift Calculation</i>	48
	4.2.2 <i>Drag Calculation</i>	49
<b>5</b>	<b>EXPERIMENTAL TESTING OF MULTI-SECTION VARIABLE CAMBER WING</b>	<b>52</b>
5.1	EXPERIMENTAL TEST APPARATUS	52
	5.1.1 <i>Wind Tunnel</i>	52
	5.1.2 <i>Test Balance</i>	53
	5.1.3 <i>Load-Cells Calibration</i>	54
5.2	TEST MATRIX AND TEST PROCEDURE	56
5.3	TEST RESULTS	58
5.4	DISCUSSION OF RESULTS	70
5.5	SUMMARY OF TEST RESULTS	72
<b>6</b>	<b>CONCLUSION</b>	<b>74</b>
6.1	CONCLUSION	74
6.2	CONTRIBUTIONS	76
6.3	FUTURE WORK	77
	<b>APPENDIX</b>	<b>78</b>
	<b>REFERENCES</b>	<b>79</b>

## LIST OF TABLES

Table 5-1: Wind Tunnel Test Matrix	56
Table 5-2: Summary of Test Results at $Re = 3.2 \times 10^5$	72
Table 5-3: Summary of Test Results at $Re = 4.8 \times 10^5$	72
Table 5-4: Summary of Test Results at $Re = 6.3 \times 10^5$	73
Table A.1: Parameter Values for Munk's Solution	78
Table A.2: Parameter Values for Pankhurst's Solution	78

## LIST OF FIGURES

Figure 1-1 Multi-Section Variable Camber Wing with Pneumatic Actuator	6
Figure 2-1 The Wright Flyer	10
Figure 2-2 Parker Variable Camber Wing	11
Figure 2-3 Burnelli's GX-3 Camber Mechanism	12
Figure 2-4 Fowler Flap	14
Figure 2-5 Types of Trailing Edge Flaps	14
Figure 2-6 Types of Leading Edge High-Lift Devices	14
Figure 2-7 Slat Actuation and Support Mechanisms on A330/340	15
Figure 2-8 Fixed Hinge Mechanism Used to Support Flap on DC9/MD80/B717	15
Figure 2-9 Four-Bar Linkage System Used to Support and Actuate Outboard Single-Slotted flap on B777	16
Figure 2-10 Link-Track Mechanism Used to Support and Actuate Single-Slotted Flap on A320	16
Figure 2-11 The MAW Smooth Variable-Camber Flap Shape	17
Figure 2-12 AAW vs. Conventional Control	19
Figure 2-13 An Experimental F/A-18 with Flexible Wings First Test Flight	19
Figure 2-14 Variform Wing Concept	20
Figure 2-15 Possible Fuel Bladder Configurations for Variform Wing	20
Figure 2-16 Buckle-Wing Biplane Concept	21

Figure 2-17 Schematic of Shape Control of Leading and Trailing Edges of an Airfoil Using Compliant Mechanisms	23
Figure 2-18 Enlarged Isometric View of THUNDER Actuator	24
Figure 2-19 Unrestrained Positive Actuation of THUNDER	24
Figure 2-20 Wing Plan-form With Separate Controlled Actuator in Each Module	25
Figure 2-21 Cross-Section Drawing of the Reconfigurable Wing	26
Figure 2-22 Reconfigurable Wing Wind Tunnel Model	27
Figure 2-23 Smart Wing Model	28
Figure 2-24 SMA Torque Tube	29
Figure 3-1 Cross-Section Drawing of the Multi-Section Variable Camber Wing	33
Figure 3-2 Miniature Threaded-Body Air Cylinder	33
Figure 3-3 Actuator Test Setup	34
Figure 3-4 Actuator Test Result	35
Figure 3-5 Pneumatic Solenoid Valve	36
Figure 3-6 Siglab Signal Generator and Pneumatic Valves	36
Figure 3-7 Polyurethane Tubes, Tube Fittings, and Pneumatic Solenoid Valves	37
Figure 3-8 Wing Rib, Collars, Music Wire, and Connection Links	38
Figure 3-9 Actuators Installed Inside the Main Spar	39
Figure 3-10 Actuation Scheme	40
Figure 3-11 Wing Structures Assembly	40
Figure 3-12 Wing with Skin	41
Figure 3-13 Baseline Rigid Wing	42
Figure 3-14 Cambered Rigid Wing	43

Figure 4-1 Cross-Section Drawing of the Model Wing in Camber Configuration and NACA9312	47
Figure 5-1 Free-Jet Wind Tunnel	53
Figure 5-2 Wind Tunnel Test Balance	54
Figure 5-3 Setup for Calibration of Test Balance	55
Figure 5-4 Lift Calibration Result	55
Figure 5-5 Drag Calibration Result	56
Figure 5-6 Lift Coefficient for Baseline Configuration at $Re = 3.22 \times 10^5$	58
Figure 5-7 Lift Coefficient for Baseline Configuration at $Re = 4.80 \times 10^5$	59
Figure 5-8 Lift Coefficient for Baseline Configuration at $Re = 6.36 \times 10^5$	59
Figure 5-9 Lift Coefficient for Cambered Configuration at $Re = 3.22 \times 10^5$	60
Figure 5-10 Lift Coefficient for Cambered Configuration at $Re = 4.80 \times 10^5$	61
Figure 5-11 Lift Coefficient for Cambered Configuration at $Re = 6.36 \times 10^5$	61
Figure 5-12 Drag Coefficient for Baseline Configuration at $Re = 3.22 \times 10^5$	62
Figure 5-13 Drag Coefficient for Baseline Configuration at $Re = 4.80 \times 10^5$	63
Figure 5-14 Drag Coefficient for Baseline Configuration at $Re = 6.36 \times 10^5$	63
Figure 5-15 Drag Coefficient for Cambered Configuration at $Re = 3.22 \times 10^5$	64
Figure 5-16 Drag Coefficient for Cambered Configuration at $Re = 4.80 \times 10^5$	65
Figure 5-17 Drag Coefficient for Cambered Configuration at $Re = 6.36 \times 10^5$	65
Figure 5-18 Lift-to-Drag Ratio for Baseline Configuration at $Re = 3.22 \times 10^5$	66
Figure 5-19 Lift-to-Drag Ratio for Baseline Configuration at $Re = 4.80 \times 10^5$	67
Figure 5-20 Lift-to-Drag Ratio for Baseline Configuration at $Re = 6.36 \times 10^5$	67
Figure 5-21 Lift-to-Drag Ratio for Cambered Configuration at $Re = 3.22 \times 10^5$	68

Figure 5-22 Lift-to-Drag Ratio for Cambered Configuration at $Re = 4.80 \times 10^5$	69
Figure 5-23 Lift-to-Drag Ratio for Cambered Configuration at $Re = 6.36 \times 10^5$	69
Figure 5-24 Wing Comparison	70

## LIST OF ABBREVIATIONS

psi	Pound per square inch
AAW	Active Aeroelastic Wing
ABS	Acrylonitrile-Butadiene-Styrene
AFTI	Advanced Fighter Technology Integration
AFW	Active Flexible Wing
AoA	Angle of Attack
CNC	Computer Numerical Controlled
DARPA	Defense Advanced Research Projects Agency
FDM	Fused Deposition Modeling
LaRC MD	Langley Research Center Materials Division
MAW	Mission Adaptive Wing
NACA	National Advisory Committee for Aeronautics
NASA	National Aeronautics and Space Administration
RAINBOW	Reduced And Internally-Biased Oxide Wafer
SMA	Shape Memory Alloys
THUNDER	THin layer composite UNimorph ferroelectric DrivER and Sensor
UAV	Unmanned Aerial Vehicle
UCAV	Uninhabited Combat Air Vehicle
VDC	Volt Direct Current

## NOMENCLATURE

$a$	Lift Curve Slope
$a_0$	Theoretical Lift Curve Slope
$a_\infty$	Speed of sound (ft/s)
$AR$	Aspect ratio, $b^2/S_{wing}$
$b$	Wingspan (ft)
$c$	Specific Fuel Consumption
$c_t$	Trust Specific Fuel Consumption (lb of fuel/hr/lb of thrust)
$c_d$	Profile Drag
$c_{d_f}$	Friction Drag
$c_{d_p}$	Pressure Drag
$c_f$	Friction Coefficient
$c_p$	Pressure Coefficient
$C_L$	Lift Coefficient
$C_{L_0}$	Lift Coefficient for minimum drag
$C_{L_\alpha}$	Lift curve slope of the wing
$C_D$	Drag Coefficient
$C_{D_i}$	Lift induced drag
$D$	Drag
$E$	Endurance of the aircraft
$L$	Lift
$L/D$	Lift-to-Drag ratio
$q_\infty$	Dynamic pressure (lb/ft <sup>2</sup> )
$R$	Range of the aircraft
$S$	Wing area (ft <sup>2</sup> )
$V_\infty$	Airspeed (ft/s)
$W$	Aircraft Weight
$W_0$	Gross weight of the plane
$W_1$	Weight with the fuel tank empty
$\alpha$	Angle of attack (radian)
$\alpha_{L=0}$	Angle of Zero Lift
$\rho_\infty$	Air density (slug/ft <sup>3</sup> )
$\eta_{pr}$	Propeller Efficiency

## **1 INTRODUCTION**

A small percentage reduction in the fuel consumption of an airplane can lead to major savings in aircraft operational costs. Since the amount of fuel stored in the aircraft is limited, lower fuel consumption means greater range or endurance in flight. There has been a great deal of research focused on achieving this goal. One promising concept is the use of a variable camber wing. This wing can change its configuration and provide variations in lift and drag that satisfy different flight conditions so fuel can be consumed efficiently.

Variable camber wing concepts have been explored and developed extensively since the beginning of flight. The wing warping of the Wright Flyer, which used the pulling of cables to change the configuration of the wing tips was considered the first variable camber wing concept. The most significant variable camber devices currently used in most transport aircrafts are high-lift devices such as leading-edge slats and trailing-edge flaps. Those devices have demonstrated very promising results in reducing fuel consumption. Throughout this thesis, a wing with high-lift devices will be referred to as a conventional variable camber wing.

In the past few decades, developments in smart materials have shown the promise of providing better actuation systems by improving aerodynamic performance of the wing and eliminating the problems associated with conventional variable camber wings such as the discontinuity on the wing surface and the excessive weight of actuation system. Research on the development of variable camber wings using smart materials<sup>1-8</sup> such as Shape Memory Alloys (SMA) and piezoelectric materials has become one of the most significant sources of interest in aerospace engineering. However, the current smart materials do not possess the capability to be used in full-scale applications. Therefore, another technique of changing the wing camber for full-scale applications must be investigated.

## **1.1 Motivation**

Even though traditional high-lift devices have shown the capability of improving the aerodynamic performance of the aircraft, these systems involve discontinuities or sudden curvature changes in the airfoil cross-section and also involve complex and bulky actuation systems. Thus, the variable camber wing concept that can improve aerodynamics properties of the plane in different flight conditions and at the same time be simple and lightweight must be investigated.

Recent research in smart materials<sup>1-10</sup> shows their potential for changing the configuration of airplane wing to improve aerodynamic performance and shows that they can eliminate the complexity and bulkiness of the actuating systems that are used in conventional variable camber wings. The general idea of changing the wing

configuration for this concept is to induce strain in the structure by interfacing with smart materials. The induction of strain in piezoelectric material is accomplished by applying the electric field to pull the monopoles in the material causing it to deflect. The relation of strain and voltage is linear in the first order. However, this is not always ideal because of the presence the nonlinear characteristics, such as depoling, hysteresis, and creep. For Shape Memory Alloys, the deformation is a result of phase transformation of material due to temperature change caused by electric field or external heating and cooling system. The SMA changes its shape upon heating process and returns to its original shape upon cooling. The phase transformation of the SMA is a nonlinear phenomenon. Even though the feasibility of using smart materials to improve aerodynamics has been demonstrated by many groups of researchers, including NASA, DARPA, and various universities, there have not been any feasible real-world applications due to limitations of smart materials' capabilities. The most serious limitations of currently available smart materials are their stroke and power, which place a practical limitation on the achievable induced strain levels. Large amounts of smart materials must be used to provide high strain level which results in the increase of system weight. Currently, the piezoelectric actuators have high bandwidth but low strain, whereas SMA actuators have relatively higher strain but extremely low bandwidth. Therefore, use of smart materials for strain actuation involves trade-offs of strain, weight, and bandwidth.<sup>9</sup> There are also other problems involving the use of smart materials for varying the wing configurations other than stroke and power. These problems are the nonlinear piezoelectric characteristics caused by depoling, hysteresis, and creep; the lack of ability to hold the deformed shape when using piezoelectric actuators; and the need of reliable feedback control techniques

to operate the actuation system. Due to these problems, a new type of actuation system must be developed to serve the actuation purpose in real flight applications.

## **1.2 Objective**

The “multi-section variable camber wing” is introduced in this research thesis to provide an effective yet simple means of changing the shape of the wing. The wing rib is divided into sections that can rotate relative to one another providing discrete but smooth change in camber. The multi-section configuration is chosen because it is convenient to vary the shape of wing because it is composed of movable parts just like humans’ fingers or limbs.

The wind tunnel model of a foot long chord is used because it provides enough space inside the wing to work with. The span of one foot is also used for the model to be placed in the 22-by-22 ft test section of the wind tunnel because the previous experiments in this wind tunnel have shown that this size of span seems to provide the best aerodynamic test results.

Since the sections are easy to rotate, no high forcing power is necessary to alter the shape. The important aspect of the actuation system is its ability to hold different shapes of the wing while in the air stream. The pneumatic actuator is chosen for actuation system because of its strength, its fast actuation time, its simplicity of control and its small size.

### **1.3 Outline**

This research focuses on designing and testing a variable camber wing model using multi-section ribs and pneumatic actuators. The model consists of four sets of six NACA0012 airfoil rib-sections connected through sub-spars, with the main spar located at one sixth of the chord of the airfoil. Due to limitation in space of the rib section the main spar cannot be placed at the quarter chord of the wing. Each section of the rib can rotate up to 5 degrees upwards or downwards without causing major discontinuity on the airfoil cross-section. The wing is actuated through small-diameter steel pushrods by two miniature threaded-body air cylinders imbedded on the main spar. The skin of the wing is made of the insignia cloth (an adhesive backed polyester fabric for making banners and flags) and latex sheet bonded together. Both materials provide sufficient strength and elasticity for the wing in both baseline and morphing configuration. Figure 1-1 shows the multi-section variable camber wing used for wind tunnel testing.



**Figure 1-1 Multi-Section Variable Camber Wing with Pneumatic Actuators**

The tests were performed in the open jet wind tunnel with a 22-by-22 ft test section. Lift and drag were measured at Reynolds numbers of 322000, 480000, and 636000, with the wing in the baseline configuration (NACA0012) and in the cambered configuration. Two rigid wings are manufactured to represent both configurations and are also tested under the same conditions. The results from the rigid wings tests are used to compare with those obtained from the variable camber wing and compare to the theoretical results.

#### **1.4 Technical Challenges**

The design concept for the wind tunnel model for this research involves many considerations, such as the smoothness during camber; the size, type, and position of wing spars in the wing; the type, number and location of actuators; and the type and

properties of wing skin materials. The change in shape while the wing is being cambered must be smooth for aerodynamic efficiency. The main spar must be large and strong enough to sustain the weight of the wing and it must be located near the aerodynamic center to avoid shearing from the moment force when angle of attack changes. Other small spars must be installed to hold the ribs together at locations where each section can rotate smoothly relative to one another. The actuator must be strong enough to alter the wing shape and to hold the wing shape against aerodynamic loads. Also, small numbers of actuators is desired to reduce weight penalty. Additionally, the actuators must be installed inside the wing so that there are no external components to spoil the flow. The wing skin materials must be flexible to allow the rib sections to move while they are being actuated, yet strong enough to sustain aerodynamic loads. Finding components to satisfy these requirements is a difficult task.

Once the design process was done, the wind tunnel models must be manufactured. The most difficult part of manufacturing was cutting the rib sections. These rib sections were machined using computer numerical controlled (CNC) machine since it involved complex curvatures which must be precise for assembly purposes. It was difficult to assemble the rib sections to the wing spars because each rib section must be aligned precisely with one another. Another delicate process for the wing model was building the two rigid wings using the foam-core and fiberglass skin. Cutting the foam-core with the hot-wire foam cutter, laying the fiberglass skin, and curing it required experience and skill.

The wind tunnel test was done on the free-jet wind tunnel with the test model setup in front of the opening section of the tunnel. The change in angle of attack was done

manually by loosening the nuts holding the main spar. This process was very time consuming. Furthermore, prior to testing, the test balance needed the replacement for the strain gage loadcells and also required recalibration. Replacing strain gages and recalibrating the balance was a very delicate process.

## **1.5 Thesis Contents**

After the review of the variable camber wing concepts in the past and present presented in Chapter 2, this thesis concentrates on the design, manufacture, and testing of a multi-section variable camber wing for use on surveillance mission unmanned aerial vehicles (UAV's).

Chapter 3 discusses the multi-variable wing wind tunnel test model including the materials, dimensions, actuation system, and the integration of wing structures and the actuation system.

Chapter 4 shows the equations for range and endurance that lead to the necessity of using variable camber wing to enhance these performances. The equations used for predicting the aerodynamics due to the change in camber of the multi-section variable camber wing are also presented.

Chapter 5 presents the wind tunnel test procedure, the apparatus used to obtain aerodynamic parameters, the aspect of the wind tunnel used to test the model, the procedure, test matrix, and the test results including the discussion of test results.

Chapter 6 provides the conclusion, emphasizes the contributions of the research underlying this thesis, and also discusses the future work for improving the model performance.

## **2 OVERVIEW OF VARIABLE CAMBER WING**

This chapter provides the historical background of variable camber wing concepts that have been introduced in the past century of flight including the contemporary research in development of the smart materials for airfoil actuation.

### **2.1 Variable Camber Wing in the Past**

Variable camber wings have been used since the beginning of flight. The wing warping of the Wright Flyer, shown in figure 2-1, by the Wright brothers can be viewed as the first practical application of a variable camber wing. This design uses a series of cables connecting the wing tips and the pilot's pedals. When the pilot pushes the pedal, the cables pull on the wing tips and the shape of the outer panel of the wing changes.<sup>11</sup> This operation provides the ability to control and maneuver the aircraft. However, due to the complexity and the strict patent enforcement by the Wrights on their technology and because this wing warping only works well for the relatively light, flexible, and low-speed aircraft, this method has not been developed to be used in the later types of aircrafts.<sup>11</sup> Furthermore, as aircraft became heavier, and used stronger and stiffer wings,

and flew at higher speeds, ailerons were developed to serve as a method in controlling the modern airplanes.

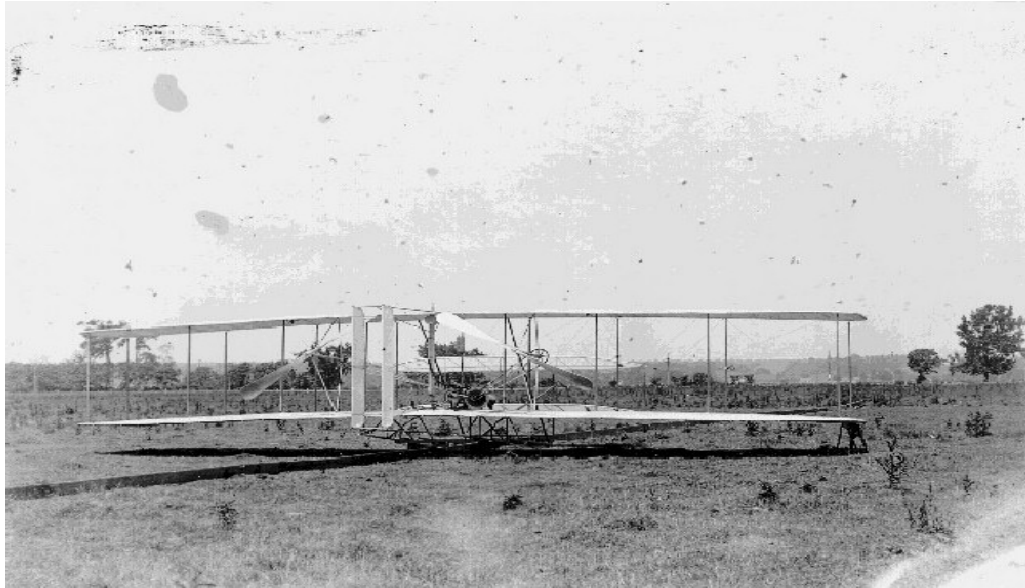


**Figure 2-1 The Wright Flyer**

In 1920, the National Advisory Committee for Aeronautics (NACA) presented a variable camber wing concept called “the Parker variable camber wing”<sup>12</sup> shown in figure 2-2. This concept involved changing the wing configuration through aerodynamic loads on the wing. This scheme divided the wing into three sections using two wing spars, one at the leading edge and the other at the two-third chord. The portion of the wing between the spars was flexible and the portion aft of the second spar was rigid. The ribs were allowed to slide over the rear spar. Thus, when the wing was placed under aerodynamic load the portion between the spars was carried upward while the rear portion being rigid and fixed to it, moved downward resulting in a camber wing. The wing was covered with fabric continuously except where the flexible channel was connected to the tailpiece, a 1-inch space was left open to allow the lower portion of the fixed tail to slide to when the

wing was deformed. The wind tunnel test results showed that the wing had a maximum lift coefficient of 0.76 and minimum drag of 0.007. However, due to the deviation in the location of center of pressure during the shape changed, this wing could lead to problems with stability control. There has not yet been any other literature about the advance research of the Parker wing found either because of the inefficiency of the wing or the patent enforcement.

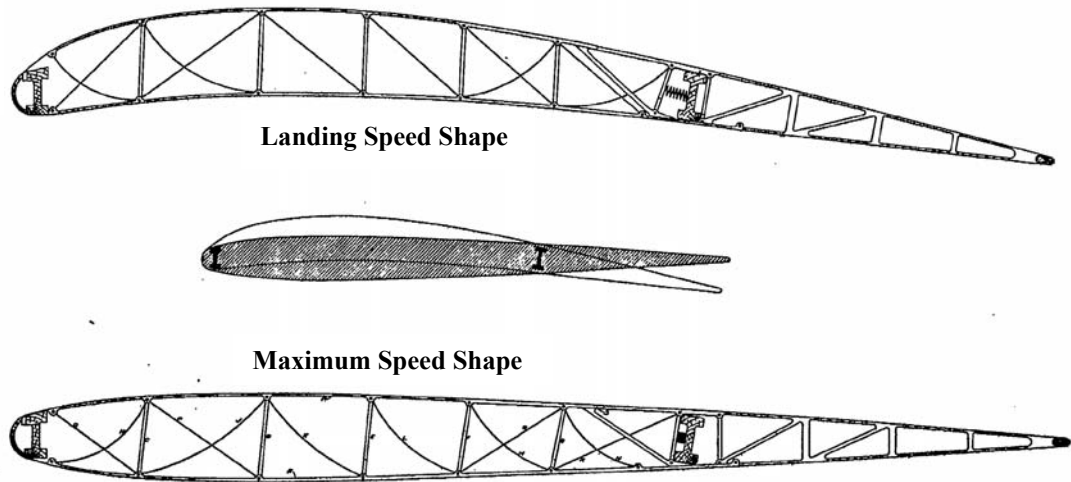


**Figure 2-2 Parker variable camber wing**

Between 1916 and 1926, Sopwith Baby Incorporated developed trailing edge flaps that could automatically deflect at lower speeds and decamber at higher speeds via a connection to restraining bungee cords. The Dayton Wright Aircraft and Army Air Service Engineering developed the same mechanism to actuate their adaptive wing and in 1933 and 1934, Westland Lysander introduced an aircraft with inboard and outboard cross-connected slates that were interconnected with trailing edge flap.<sup>5</sup>

In the safe airplane competition trails at Mitchell field on Long Island 1930, one entry called the Burnelli GX-3 was presented<sup>13</sup>. This plane featured four-wheel landing gear and a variable camber wing which made it the most distinguished aircraft in the competition. The variable camber wing on the GX-3 was developed by Burnelli and Wilford. It was a medium thickness wing that had the portion between the spars rigidly mounted and braced. The nose and trailing edge portion moved outward and downward by a rack and pinion mechanism with pinion gears mounted every five feet on to the torque shafts running parallel to the spars. The torque shaft running parallel to the forward spar was controlled by a hand wheel in the cockpit while the one running parallel to the rear spar was driven by the chain from the forward one. The pinion gears actuated curved rack members which were attached to the movable nose and trailing edge. These rack members were mounted on rollers and guidance where their curvature provided the necessary change in camber of the wing. Figure 2-3 illustrates the camber mechanism of Burnelli GX-3. After the presentation, the Burnelli monoplane was returned for modification and did not appear for the competition.

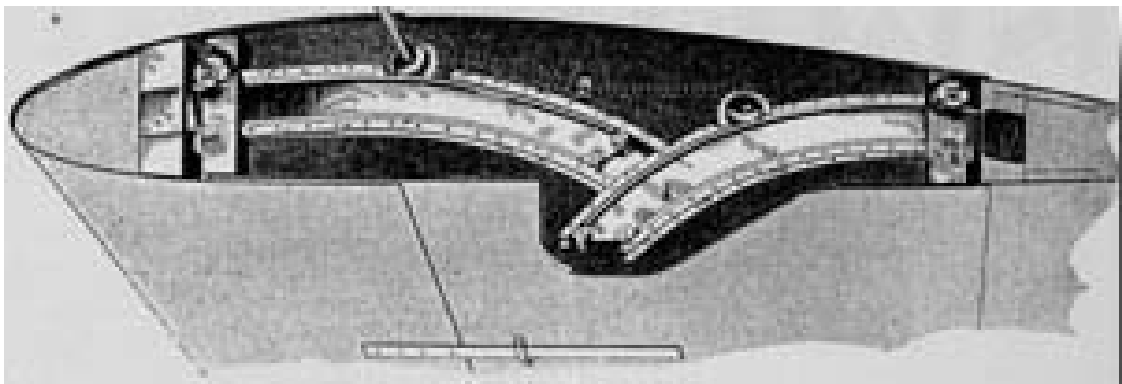


**Figure 2-3 Burnelli GX-3 Camber Mechanism**

## **2.2 Contemporary variable camber wing and concepts**

### **2.2.1 High-Lift Devices**

The High-Lift devices<sup>14-19</sup> such as leading edge slats and trailing edge flaps were introduced not too long after the first flight in 1903. Ailerons, developed in 1908 were the first type of flaps that used to provide lateral control of the plane. Flaps were first introduced in 1914 on the British S.E.-4 biplane but they were rarely used because the increase in performance was very small. The flaps idea remained insignificant until Orville Wright and J.M.H. Jacobs invented the “split flap” in 1920. It consisted of a hinged section on the trailing edge of the underside of the wing as shown in figure 2-5, which helped the plane to descend toward the runway at a steeper rate due to the increase in drag. Several years after the flaps were presented, the idea of the slotted wing, a long slot that runs lengthwise along the wing either at the leading edge or trailing edge, was investigated simultaneously by two Germans working individually named G.V. Lachman and O. Mader and by one British team named Handley Page Firm. Their research showed that the lift of the wing could be improved through the slotted wing but the drag was also increased. In the mid-1920s, Harland D. Fowler, developed a so-called “fowler flap,” shown in figure 2-4, combining the slots and flaps to increase the wing’s lift. The double-slotted flap, shown in figure 2-5, which was simpler and lighter than fowler flap, was invented later in 1937 by an Italian company named Piaggio.<sup>14</sup> The development in leading edge and trailing edge devices has been enormously increased and has been used effectively to improve the performance of modern airliners. Some of the trailing edge

flaps and leading edge high lift devices are illustrated in figure 2-5 and figure 2-6 respectively.

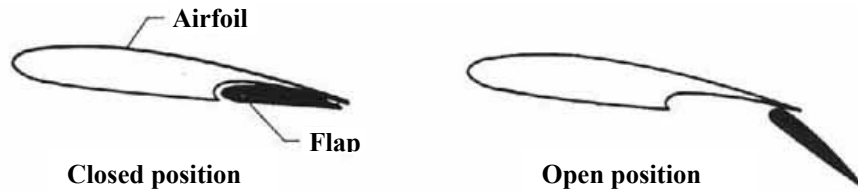


Figure 2-4 Fowler Flap

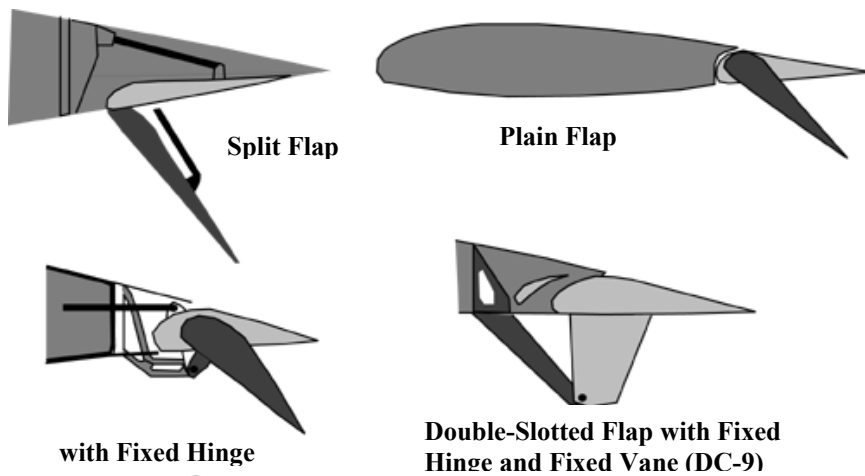


Figure 2-5 Types of Trailing Edge Flaps

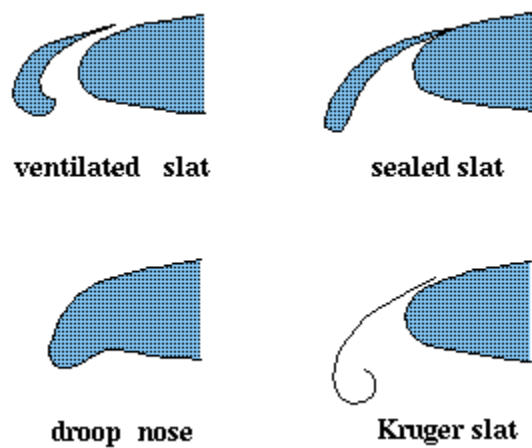


Figure 2-6 Types of Leading Edge High Lift Devices

Even though the high lift devices have shown promising improvements in aerodynamic performance, these devices were driven by rather complex and bulky actuation systems such as the rotary actuator, a pneumatic device with a rotary output, used to actuate the slats, fixed hinge mechanism, four-bar linkage system, and link-track mechanism.<sup>15</sup> These actuation and supporting devices are shown in figure 2-7, 2-8, 2-9, and 2-10 respectively.

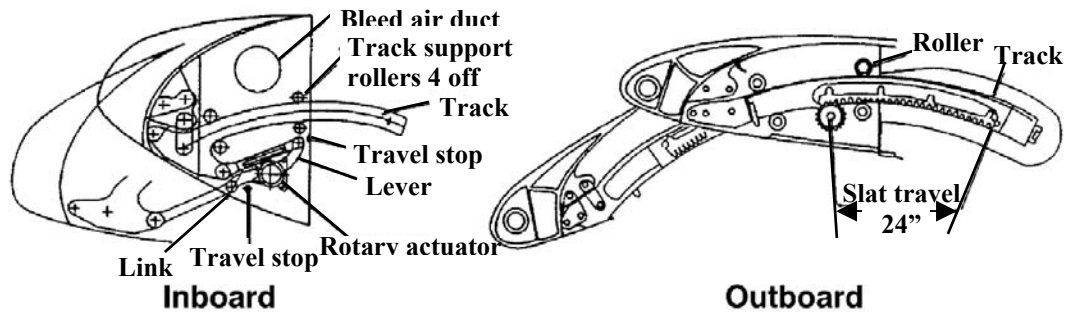


Figure 2-7 Slat Actuation and Support Mechanisms on A330/340

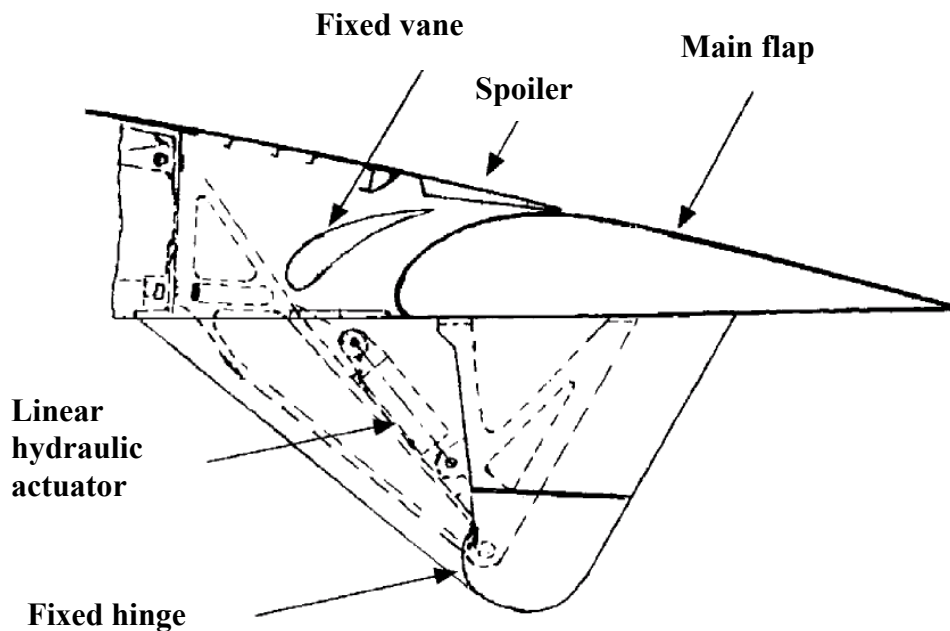
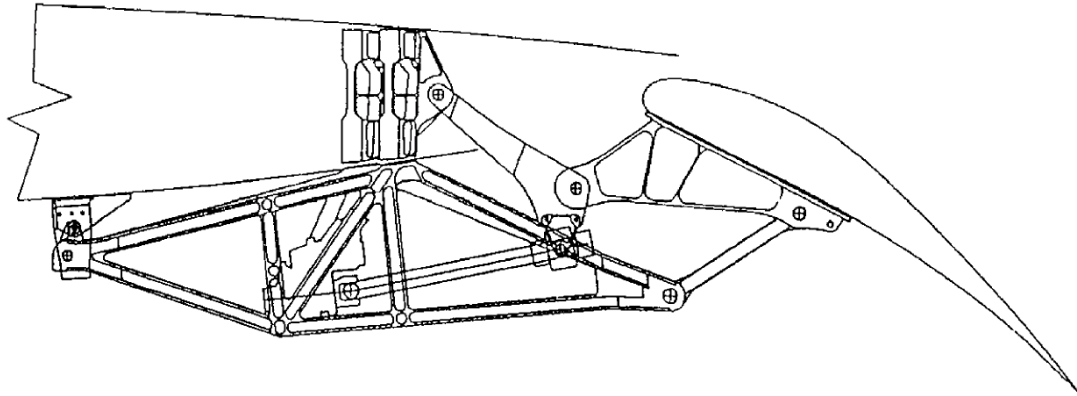
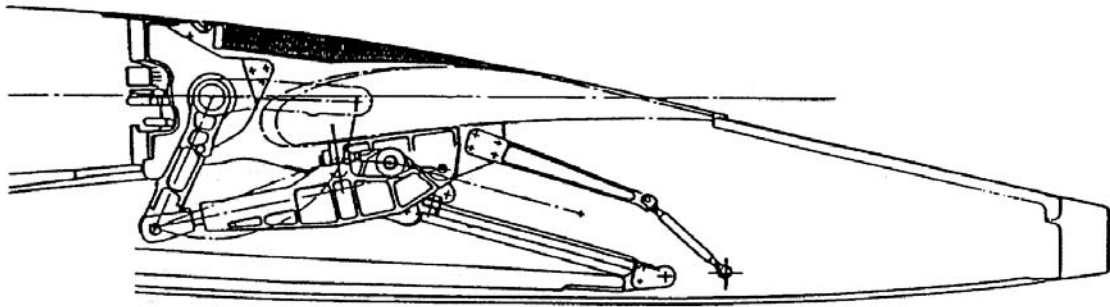


Figure 2-8 Fixed hinge mechanism used to support flap on DC9/MD80/B717



**Figure 2-9 Four-Bar linkage system used to support and actuate outboard single-slotted flap on B777**



**Figure 2-10 Link-Track mechanism used to support and actuate single-slotted flap on A320**

## **2.2.2 Mission Adaptive Wing (MAW)**

In 1985, the Mission Adaptive Wing<sup>19,20</sup> (MAW) concept was introduced and tested on an F-111 by the joint program between NASA's Ames-Dryden Flight Research Facility and the U.S. Air Force called Advanced Fighter Technology Integration (AFTI). The MAW wing, built by Boeing Aircraft Company System, consisted of leading and trailing edge variable-camber surfaces that could be deflected in flight to provide a near-ideal wing camber shape for any flight condition using an internal mechanism to flex the outer wing skin. The upper surface of the wing was continuous and flexible whereas the lower surface was fully enclosed. Thus, the leading edge slats and trailing edge flaps

were eliminated. The wing system had four automatic control modes: (1) Maneuver Camber Control - adjusting camber shape for peak aerodynamic efficiency; (2) Cruise Camber Control – for maximum speed at any altitude and power setting; (3) Maneuver Load Control – providing the highest possible aircraft load factor; (4) Maneuver Enhancement Alleviation – in part attempting to reduce the impact of wing gusts on the plane ride. The AFTI/F-111 with MAW system was flown 59 flights from 1985 through 1988. The flight test data showed a drag reduction of around 7 percent at the wing design cruise point to over 20 percent at an off-design condition. The four automatic modes were tested in flight with satisfactory results.<sup>20</sup> Figure 2-11 shows the mission adaptive wing in F-111.

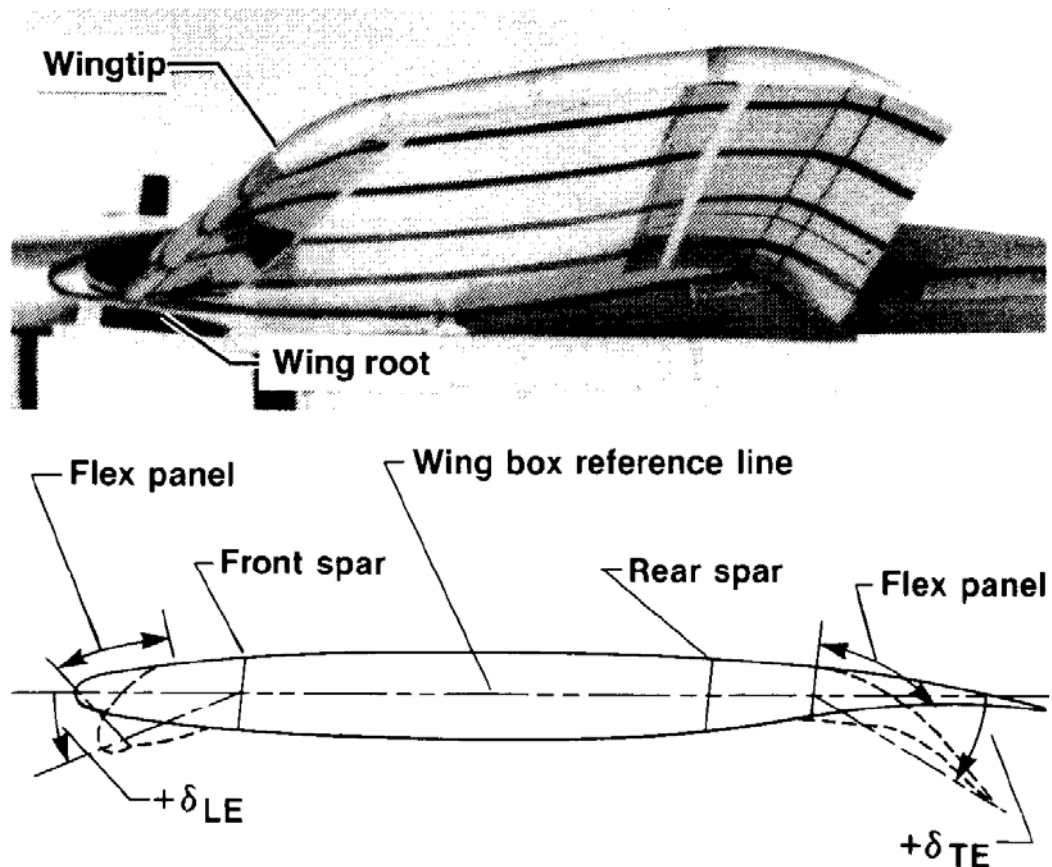


Figure 2-11 The MAW Smooth Variable-Camber Flap Shape

### **2.2.3 Active Aeroelastic Wing (AAW)**

The Active Aeroelastic Wing<sup>21-26</sup> (AAW) concept, also known as Active Flexible Wing (AFW) concept was introduced in the 1980s by Rockwell International Corporation as a means to solve the aeroelastic control reversal problem in multi-point tactical fighter aircraft designs. This wing concept had been developed extensively by DARPA, US Air Force, Boeing, and NASA for use on fighter aircraft. The idea of the AAW concept was based on the wing warping of the Wright Flyer but instead of using a series of cables to twist the wing for control purposes, AAW used the aeroelastic torque to twist the wing to provide control forces through the deflection of multiple leading and trailing edge control surfaces. Even though the control surfaces on the AAW could provide control forces, they were not a primary source of controlling the aircraft as in conventional wings therefore these wings could be operated beyond the reversal speeds. Unlike conventional wings which suffered the structural weight and drag penalties because they are stiff and rigid to avoid the degradation in control effectiveness due to the flexibility of the wing caused the adverse aeroelastic twist, AAW technology requires a more flexible and thinner wing thus a lighter and lower drag airplane can be achieved. Figure 2-12 illustrates the differences between AAW technology and the conventional control approach. The AAW technology is twisting in the positive way with the use of both trailing edge and trailing edge surfaces whereas the conventional wing with only trailing edge is twisting in negative way causing the adverse twist, which reduces the control surface effectiveness and causes control surface reversal. Figure 2-13 shows the experimental F/A-18 flexible wings taking off on its first test flight from NASA Dryden at Edwards Air Force Base, California on November 15, 2002.

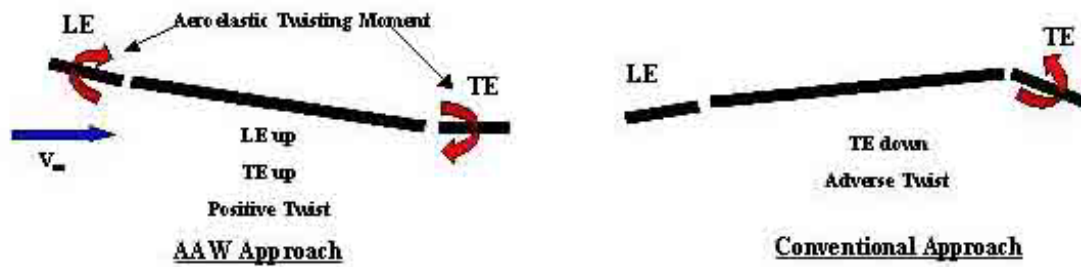


Figure 2-12 AAW vs. Conventional control.



Figure 2-13 An Experimental F/A-18 with Flexible Wings First Test Flight

## 2.2.4 Variform Wing Concept and Buckle-Wing Biplane

The Department of Aerospace and Mechanical Engineering at the University of Notre Dame introduced new variable wing concepts called “variform wing”<sup>27</sup> in 2002 and “buckle –wing biplane”<sup>28</sup> in 2003, to enhance the aerodynamic performance of Unmanned Aerial Vehicles (UAV’s) and Micro Aerial Vehicles (MAV’s).

The approach to the variform wing concept is to store fuel in the balloon-like bladders inside the wing interacting with the wing structure. As the fuel is consumed, the bladders shrink which deforms the shape of the wing. Figure 2-14 illustrates the variform wing concept; the outer profile indicates the airfoil shape when the bladders are filled and the solid-filled shaped represents the airfoil configuration when the bladders are empty. Figure 2-15 shows the possible shapes of the bladder inside the variform wing concept. There has not yet been any further investigation done on this wing concept but range and endurance were theoretically estimated to increase.



**Figure 2-14 Variform Wing Concept**



**Figure 2-15 Possible Fuel Bladder Configurations for Variform Wing**

The “buckle-wing biplane” concept was a unique variable camber wing. There is no internal actuator required inside the wing reducing the problem of actuator installation. The wing consisted of a stiff lower lifting surface joined in the outboard regions with a highly elastic upper lifting surface that can be elastically buckled to provide higher aspect

ratio, lower wing loading, and provide significant change in wing profile. Two outboard actuators and one center actuator were required to provide axial load and transverse load to separate the two lifting surface respectively. Figure 2-16 shows the cross-section of the buckle-wing biplane when both wings are separated and when they are combined including the integration of the wing to the aircraft. The research for this wing concept is still on going because the interaction of the fluid between the two surfaces must be studied. Furthermore, the shape of both wings must be investigated in greater detail to be able to produce optimum lift and minimum drag since the drag can be generated from both surfaces while separating and form the discontinuity on the surface while combining.

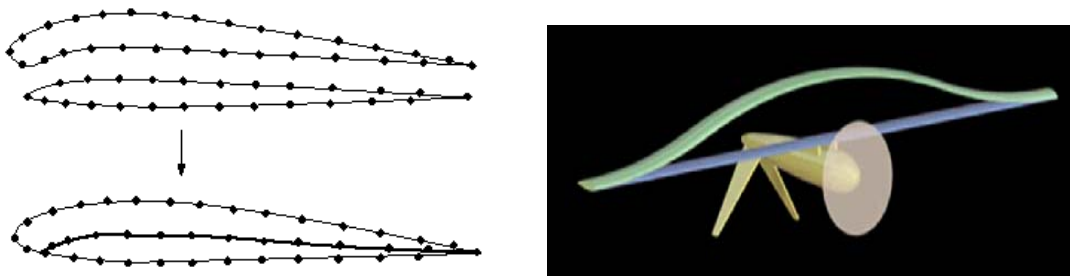


Figure 2-16 Buckle-Wing Biplane Concept

### 2.3 Smart materials and variable camber wing

The development of smart materials has become the main focus of variable camber wing actuation technology today. Piezoelectric materials and Shape Memory Alloys have shown some possibilities to be used as actuators for deforming the wing profile. Followings are some variable camber wing concepts that have been investigated.

### 2.3.1 Compliant Mechanism

The current smart materials that have been developed do not have the capability to serve the actuation purpose in full-scale models since the displacement and force obtained from individual actuators are extremely low. In order to achieve better actuation forces, a large amount of material must be used causing the model to suffer weight penalty. The actuation concept called “compliant mechanisms,”<sup>9</sup> developed at the University of Michigan, was introduced in 1999 showing the possibility of using small amounts of existing smart materials to achieve the desired deformation. Through this concept, the change of the wing shape was accomplished by transmitting controlled displacements and energy from the smart material installed at a convenient location away from the deforming structure through sets of flexible links and joints called “compliant mechanisms” as shown in figure 2-17. The compliant mechanisms achieve the mobility through elastic deformation of one or more of their constituent segments. They can be arranged in such a way that any small input torque, such as that from the smart materials can be used to deform the wing. Furthermore, the compliant mechanisms have several advantages over the traditional mechanisms such as lighter weight; no assembly; and freedom from backlash, friction, and noise.<sup>9</sup> Additionally, with the compliant mechanisms concept, the small actuator such as smart materials can be completely enclosed within the contour of the airfoil shape providing smooth wing surface. Since the actuator can be placed away from the structure, it can be protected from undesired effects such as being exposed to unstructured environment and stress concentrations on the structure. This concept seems viable for full-scale applications but there has not been any further investigation to validate this approach.

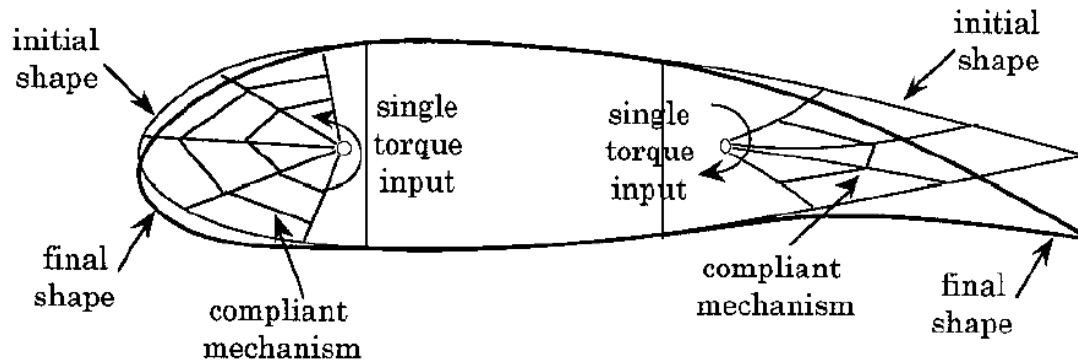


Figure 2-17 Schematic of shape control of leading and trailing edges of an airfoil using compliant mechanisms

### 2.3.2 Piezoelectric Actuator and Variable Camber Wing

Recently, researchers at NASA Langley Research Center Materials Division (LaRC MD) have developed two high-displacement piezoelectric actuators called, RAINBOW (Reduced And Internally-Biased Oxide Wafer) and THUNDER (THin layer composite UNimorph ferroelectric DrivER and sensor).<sup>5</sup> These two actuators can deform out-of-plane under applied voltage more than other types of existing piezoelectric actuators. Both RAINBOW and THUNDER are made by bonding piezoelectric wafers to metallic substrates and can be actuated by applied voltage across the wafer which forces the metallic substrate to move with it, resulting in an axial buckling and out-of-plane displacement. However, both actuators are made differently during the prestressing of fabrication process causing them to possess slightly different displacement capability. As tested<sup>5</sup>, a 1.5-in-wide, 2.5-in-long, 0.012-in-thick, 9-layer-aluminum THUNDER possesses 13 times displacement capability of a 1.25-in-diameter, 0.02-in-thick RAINBOW. Figure 2-18 shows the enlarged isometric view of the THUNDER actuator and figure 2-19 shows the unrestrained positive actuation of THUNDER.

A sub scale airfoil model was constructed to study the possibility of using THUNDER actuator attached to the upper surface of the airfoil to enhance the aerodynamic performance. The results indicated that the displacements of the upper surface of the airfoil depended on the applied voltage, airspeed, angle of attack, and the creep and hysteresis of the actuator. The force output from the actuator was greater than the aerodynamic load at all times which showed that THUNDER can be used to alter the shape of airfoil under aerodynamic load.<sup>5</sup> However, more research is still needed before the THUNDER can be applied to full-scale application.

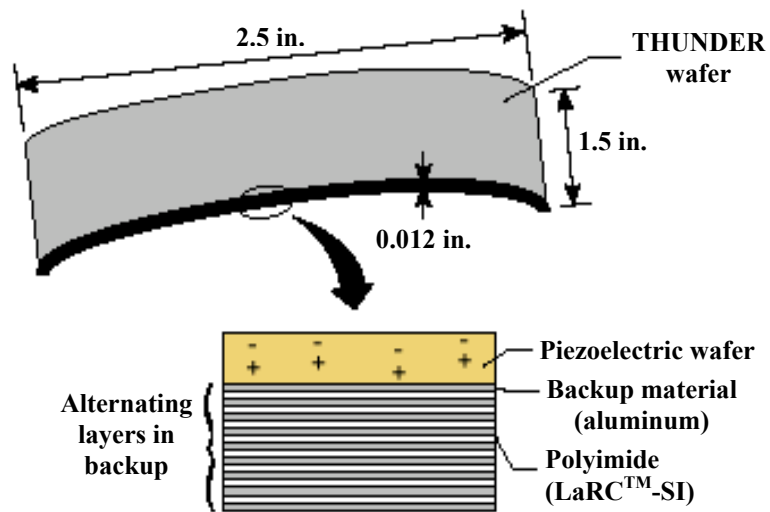


Figure 2-18 Enlarged Isometric View of THUNDER Actuator

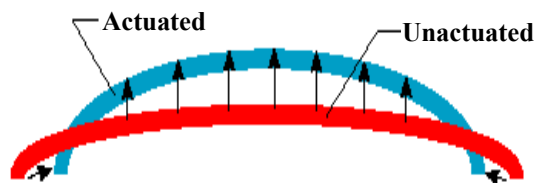
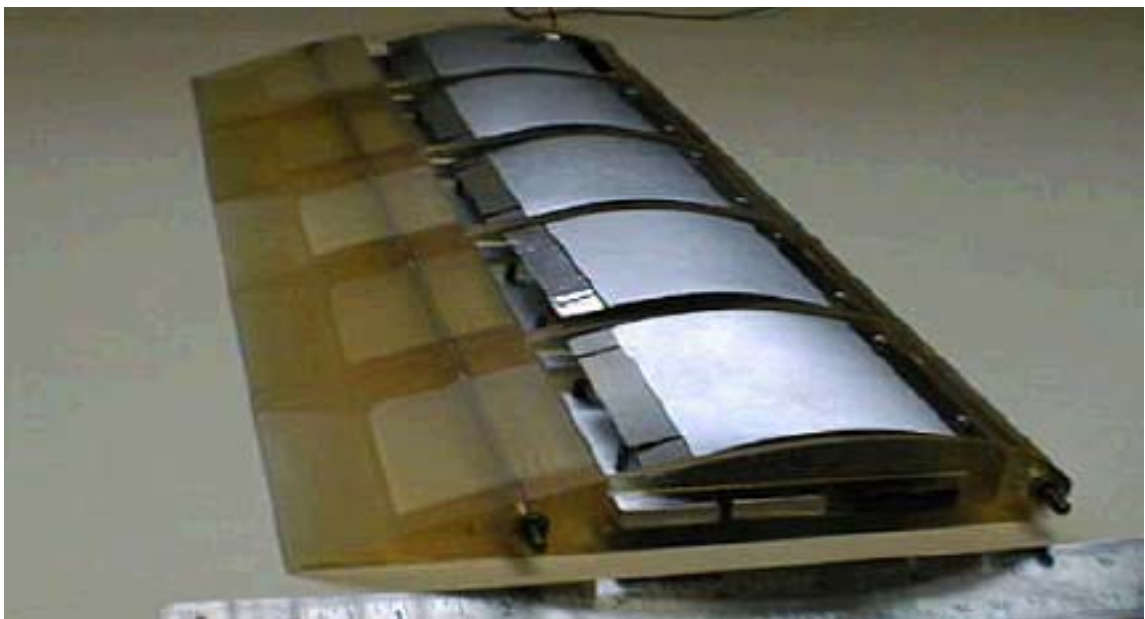


Figure 2-19 Unrestrained Positive Actuation of THUNDER

The Department of Mechanical Engineering at the University of Kentucky has also been investigating the use of THUNDER to alter the wing shape for flow control and to improve the aerodynamic performance of the wing.<sup>1-4</sup> Their wing model is a NACA4415-based airfoil similar to that of NASA at Langley Research Center except it is a modular wing with each module having a recess cut in the upper surface to install the actuator and can be added or removed to vary aspect ratio. This wing model is shown in figure 2-20. The results from their experiments show that an airfoil with oscillating camber will produce higher lift coefficient than the same airfoil at any fixed camber setting. The wind tunnel test results also show that the size of separation is reduced when the actuator is oscillating.



**Figure 2-20 Wing Plan-form With Separate Controlled Actuator in Each Module**

### 2.3.3 Reconfigurable Wing

Beside piezoelectric materials, there is another type of smart material that is being considered for use as an actuator for altering the shape of the airfoil. Shape memory alloys (SMA) exhibit unique thermal and mechanical properties. When SMA wires are properly trained, they can be used as a linear actuator by contracting when heated and returning to their original shape when cooled. The Aerospace Engineering Department at Texas A&M University has been investigating the feasibility of using SMA wires to change the shape of the wing in the past few years. Their variable camber wing concept called “reconfigurable wing”<sup>6</sup> using SMA wires as an actuator has been designed and fabricated for study. The wind tunnel model wing is a symmetric airfoil base with the wing skin made of ABS plastic, plastic based on acrylonitrile-butadiene-styrene copolymers, through the fused deposition modeling (FDM) process. Eight well-trained SMA wires were used to actuate the wind tunnel model. The cross-section drawing of the reconfigurable wing and the wind tunnel model are shown in Figure 2-21 and 2-22 respectively. When this model is fully actuated a trailing edge deflection of approximately 6 mm is obtained. The wind tunnel test results show that the lift coefficient increases when the wing is deformed.

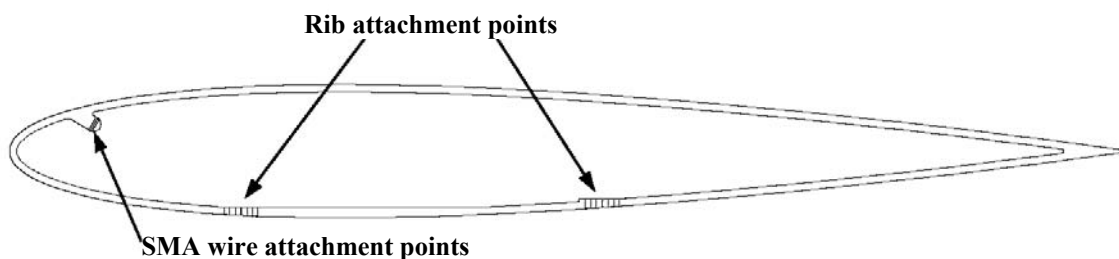
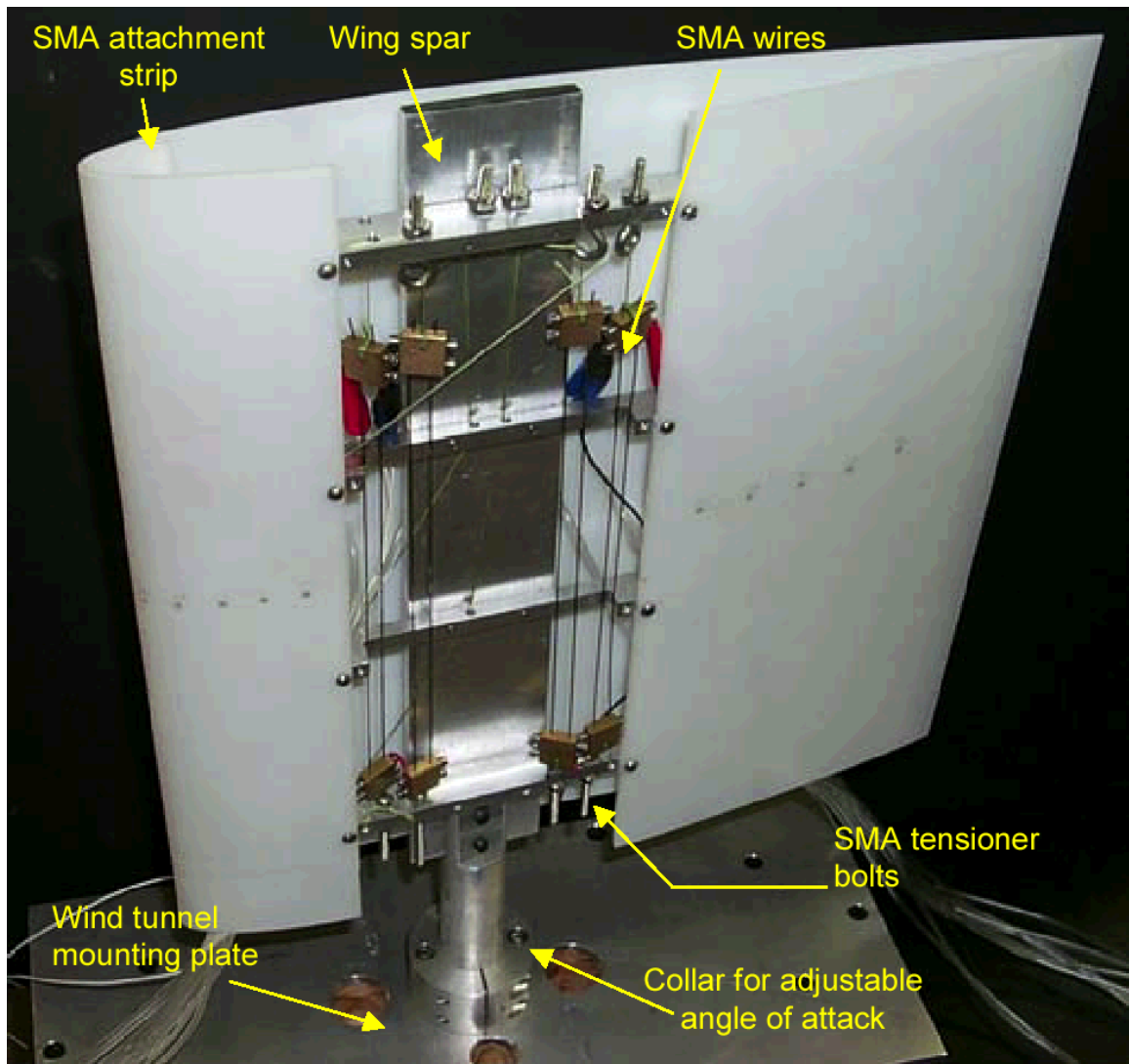


Figure 2-21 Cross-Section Drawing of the Reconfigurable Wing



**Figure 2-22 Reconfigurable Wing Wind Tunnel Model**

### **2.3.4 DARPA/Wright Lab “Smart Wing”**

The use of shape memory alloy for altering the wing shape has also been investigated by DARPA. The “smart wing”<sup>29,30</sup> has been designed, fabricated, and tested to study the potential of improving the aerodynamic properties to be used in the Uninhabited Combat Air Vehicle (UCAV).<sup>31,32</sup> The wing model, shown in figure 2-23, was based on both AFW and MAW wing designs but used improved smart materials and smart structures

technologies. The wing uses a shape memory alloy (SMA) torque tube, shown in figure 2-24, to provide wing twist inboard and outboard. The trailing edge is embedded by the SMA wires in the top and bottom face sheet to provide smooth contoured control surface. The tip deflection of about 1.25 degree is obtained from the torque tube. The wind tunnel test results show a significant improvement in pressure distribution due to delayed flow separation at the trailing edge. The increase in rolling moment between 8 and 18 percent over the conventional wing design is also observed.

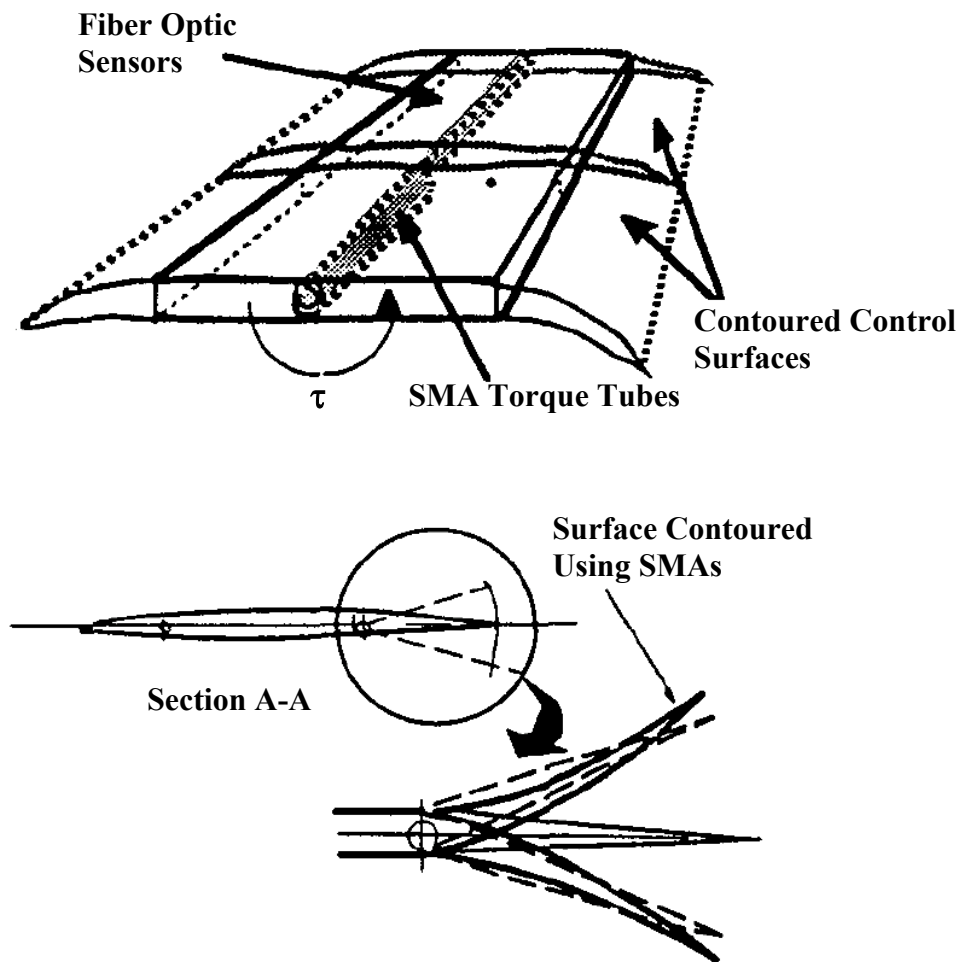


Figure 2-23 Smart Wing Model

(a) Nested Torque Tubes

(b) Twin Nested SMA Torque Tubes

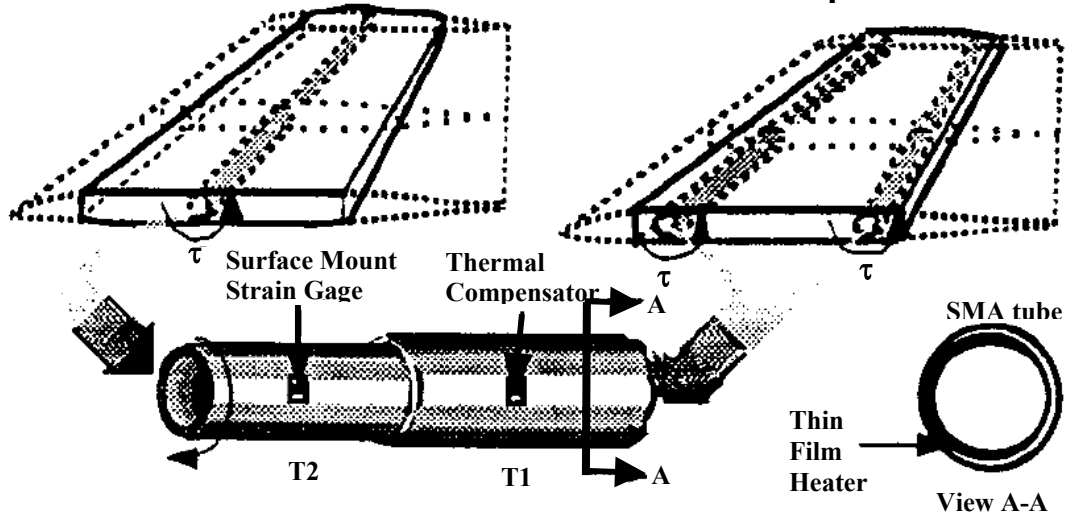


Figure 2-24 SMA Torque Tube

### **3 VARIABLE CAMBER WING DESIGN**

Three wind tunnel models were constructed for this research: one multi-section variable camber wing and two rigid wings of the baseline configuration and of the cambered configuration of the variable camber wing. Detailed information of these wing models are described as follows.

#### **3.1 Initial Concept**

The initial inspiration of this wing concept began with the desire to change the camber of the wing by deflecting only the leading edge and trailing edge portion of the wing without having any gap between each portion. Using a three-section wing concept, the wing did not provide smooth change during cambered configuration, therefore the idea of creating more sections out of the wing rib to provide discrete but smooth change in camber was introduced. The wing rib was first divided into eight sections but due to the space in the trailing edge section being too small to work with, only six sections were used instead. Dividing the wing into section provided ease in varying the shape of the airfoil since each section could rotate freely relative to the near by sections.

The idea of shape memory alloy to actuate the wing was first introduced but it was decided that SMA was infeasible due to the nonlinear property of the SMA wire and because the wing needed to be both pushed and pulled to obtain the desired configuration. A linear actuator was also considered as an actuation system but due to the difficulty in installing the component and the complication of its control system, this actuation idea was not applied. Due to the other ongoing research in morphing wing projects at the University of Maryland, such as the sweep wing and telescopic wing, using the pneumatic actuator as an actuation system and due to the simplicity of controlling system for pneumatic actuator, it was introduced as actuation system for this research. Once the actuator was decided, the components to be used along with this actuation system were investigated. The use of simple linkages system with pushrods seemed to work well with the pneumatic actuator and this entire actuation system could be embedded inside the wing. A detailed description of the final variable camber wing design is discussed in the next sections.

## **3.2 Multi-Section Variable Camber Wing**

### **3.2.1 Wing Ribs and Spars**

The wind tunnel model was a 12-inch span and 12-inch chord NACA0012-based airfoil with 4 wing ribs. Each rib was divided into 6 sections with circular cuts at both ends except for the leading and trailing edge sections, which had a circular cut at only one end. Each rib section except for the second section had a  $\frac{1}{4}$ -inch diameter hole for inserting the  $\frac{1}{4}$ -inch sub-spars; the second section from the leading edge had  $\frac{5}{8}$ -inch diameter hole for a  $\frac{5}{8}$ -inch diameter main spar and another  $\frac{1}{4}$ -inch hole for inserting a

1/4-inch stainless tube for rigidity of this section. Due to space limitations, the main spar was not located at the quarter-chord, but instead at the 1/6-chord location.

The ribs were made of aluminum and the spars were made of stainless steel tubes. Each rib section and the corresponding spar were secured together by setscrews, which allowed for convenient adjustment. Custom-made aluminum links were used to connect the rib sections together and allowed them to rotate freely. Each rib section could rotate up to 10 degrees around its own spar without providing significant discontinuity in the wing surfaces.

The process of wing rib fabricating began with determining the suitable number rib sections and the location of main spars and sub-spars. The circular curves were then created by having a center at the center of the spar location and had a radius of 0.1 inch less than the distance between the center of the spar and the point on the contour of the airfoil perpendicular to the camber line. Each section of the ribs was cut with the CNC machine. Two generations of the rib sections were fabricated, the first generation had eight rib sections and the second generation had six rib sections. The first generation provided smoother change in camber than the second generation. However, the trailing edge section of the first generation was extremely small which did not provide enough space for the actuator thus the second generation was selected for the wind tunnel model. With six rib sections, the main spar location was chosen at 2-in aft of the leading edge, which is 1/6 of the chord. The sub-spars aft of the main spar were 2 inches apart where the one in front of the main spar was located 1-1/4 inch from the main spar. Figure 3-1 shows the drawing of wing rib cross-section.

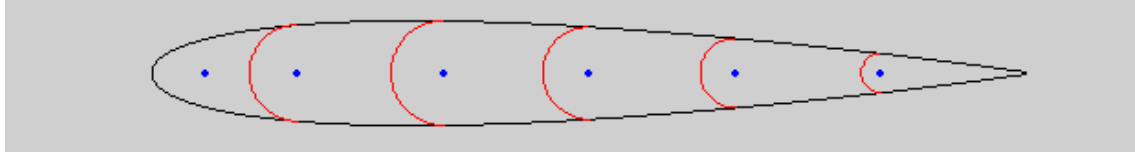


Figure 3-1 Cross-Section Drawing of the Multi-Section Variable Camber Wing

### 3.2.2 Actuators

Two miniature double acting threaded-body air cylinders with  $\frac{1}{2}$ -inch maximum stroke, shown in figure 3-2, were used to actuate the wind tunnel model. The actuator was a  $\frac{1}{2}$ "-32 body thread with overall retracted length (labeled A) of 1.99 inches. Each actuator provided a push-force of 11 lbs and pull-force of 8.6 lbs at 100 psi, and could sustain a maximum pressure of 125 psi.<sup>35</sup> This actuator was selected over an electric motor servo because of the ability to provide a higher actuation force and faster actuation time while remaining small enough to fit inside the airfoil section. However, unlike a motor servo this type of actuator could not provide intermediate displacement.

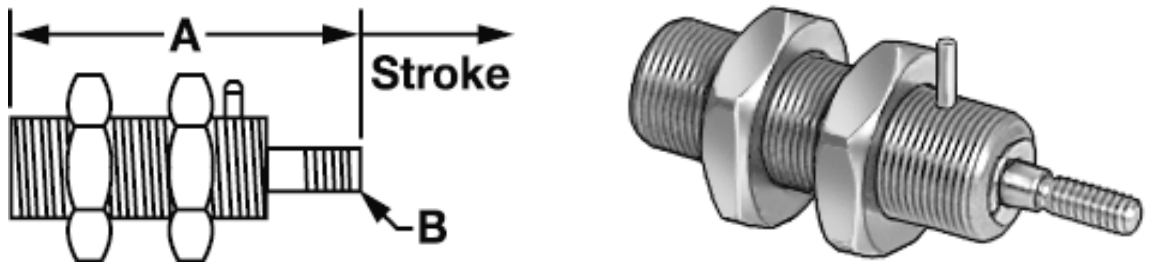
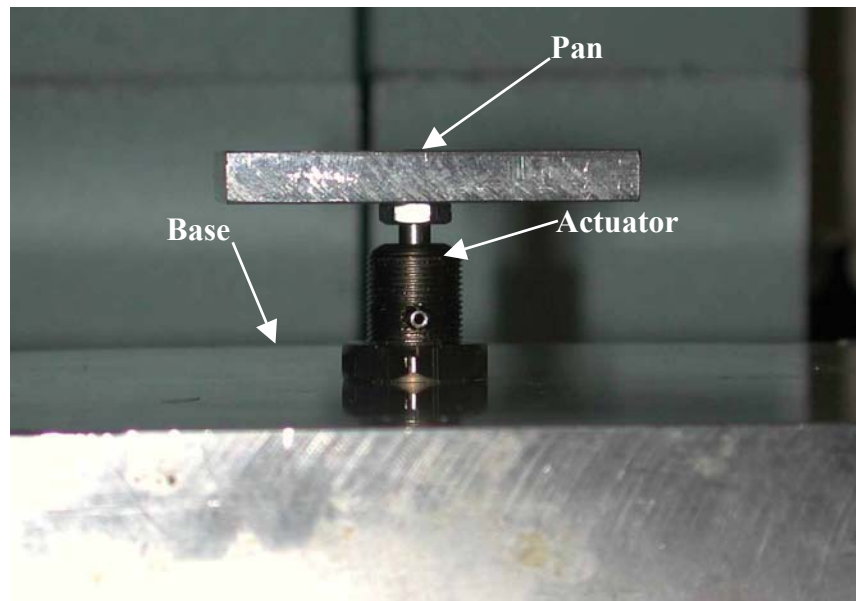


Figure 3-2 Miniature threaded-body air cylinder

The actuator was tested for its ability to sustain loads at different applied pressure. This was done by securing the actuator with a rigid base then applying known weights to the actuator one at a time until the actuator failed for each pressure input from 20 psi to

100 psi. Figure 3-3 shows the setup for actuator testing. The results, shown in figure 3-4, indicate that the maximum load that the actuator can sustain increases as the pressure increases. The maximum load at 100 psi is 10 lbs. However, the pressure at 80 psi is used for actuating the wind tunnel model during test because the leakage starts occurring as higher pressure.



**Figure 3-3 Actuator Test Setup**

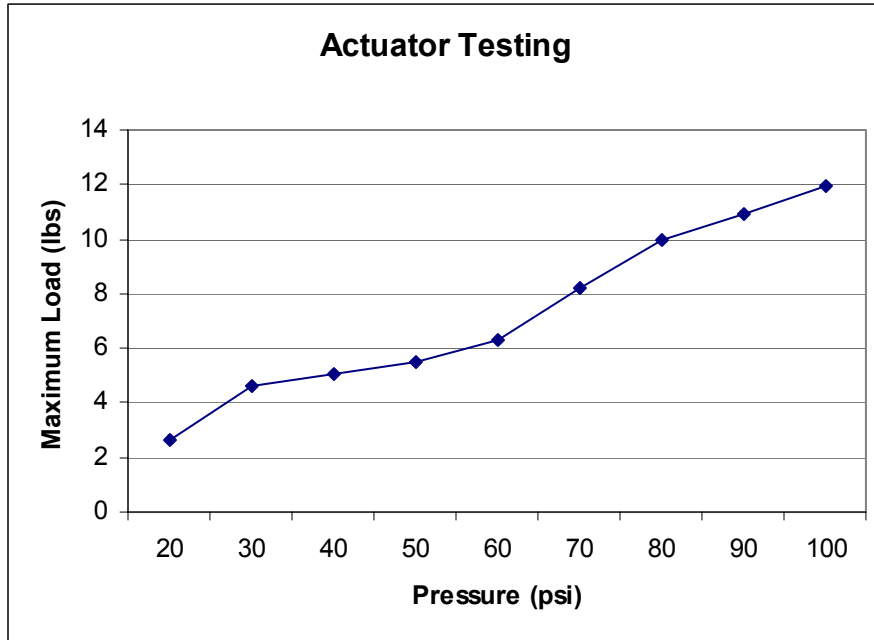


**Figure 3-4 Actuator Test Result**

The operation of the actuator requires four 12-VDC miniature electronic-operated pneumatic solenoid valves, shown in figure 3-5, to control the air intake and out-take for the actuator. These valves were 2-way normally closed and had a response time of 5-10 milliseconds. The operating pressure of the valves was 0 to 105 psi.<sup>36</sup>The constant electric field of 10 volts to control the operation of the valves was provided by a Siglab signal generator. This signal generator could provide voltages of up to  $\pm 10$  Volts. The Siglab unit and the valve connection sequence are shown in figure 3-6. The air pressure for the actuator was generated by a Newport air compressor capable of generating air pressures up to 230 psi. The Ether-base polyurethane tubes having 1/4-inch and 1/8-inch diameters and pneumatic tube fittings were used to connect the compressor, valves, and the actuators. Figure 3-7 shows the tubes, tube fittings, and the solenoid valves.



Figure 3-5 Pneumatic Solenoid Valve



Figure 3-6 Siglab signal generator and pneumatic valves

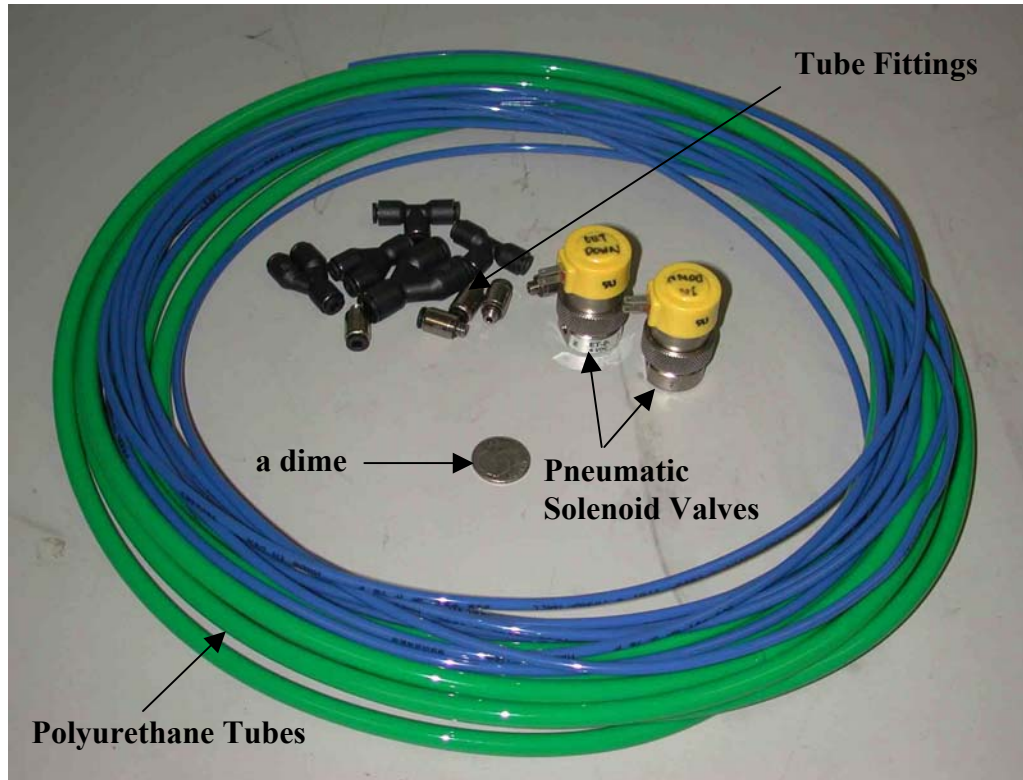
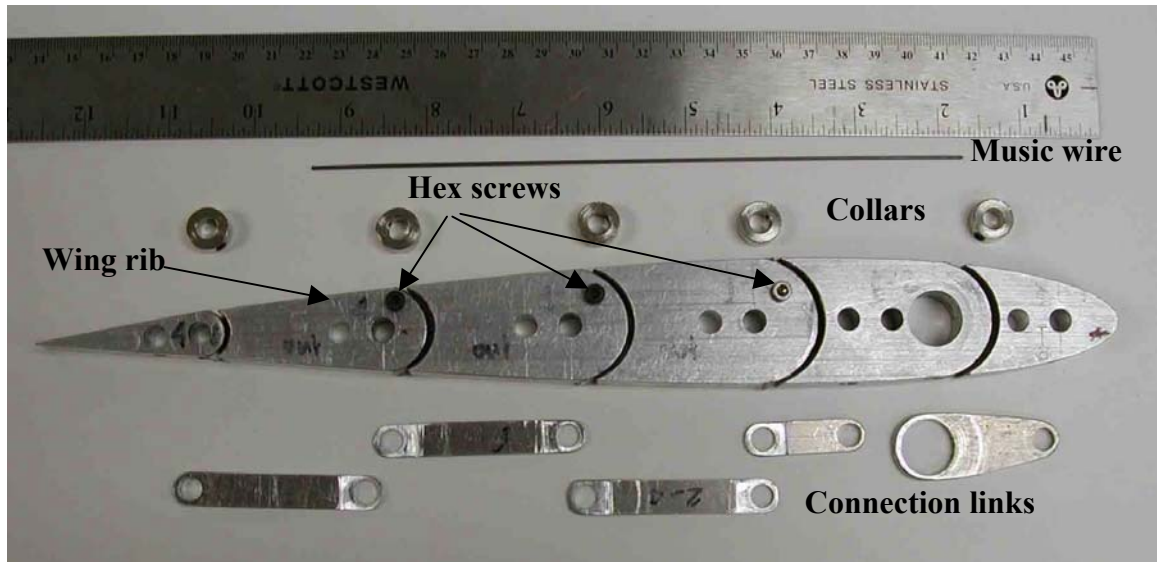


Figure 3-7 Polyurethane Tubes, Tube Fittings, and Pneumatic Solenoid Valves

### 3.2.3 Wing structures assembly

The rib sections are connected together by the chain-like connection links, which allow each section to rotate around its own spar and to rotate relative to the nearby sections. The ribs and the links are secured together by zinc plate collars. The main spar is 5/8 inches outside diameter with one end threaded for test balance mounting purpose. The sub-spars are 1/4 inches outside diameter. Two 1/16-in music wires are inserted through the sub-spars aft of the main spar to provide smooth change in curvature when the wing is actuated and to keep the alignment of the sub-spars straight when the wing is at the baseline configuration. The music wires also served as a spring, assisting the

actuators to pull the wing back to baseline configuration. Figure 3-8 shows the rib sections, connection links, music wires, and zinc-plated collars.



**Figure 3-8 Wing rib, collars, music wire, and connection links**

Four ribs are used for the wing, located such that the space in the middle of the wing was largest for installation of the actuators. The two actuators are installed inside the main spar at 2-1/4-in apart from each other and secured to the main spar with jam nuts as shown in figure 3-9.

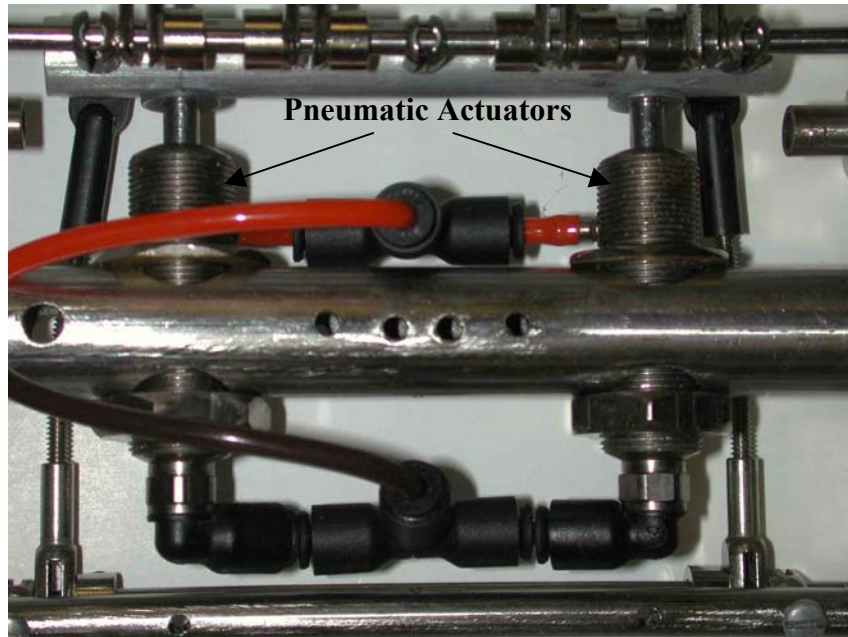


**Figure 3-9 Actuators installed inside the main spar**

Six small steel rods were used as actuation arms, two of these rods are 4-40 threaded steel rods for actuating the leading edge section, two other rods are 1/8-in stainless steel rods for actuating the trailing edge section and the last two are 4-40 steel rods for enforcing the mid-section to reduce the play movement within the wing. The four rods that are used to actuate the leading and trailing edge are slightly bent to avoid contact with the spars. Hex screws are installed into the inside rib sections of two outside ribs to serve as a stopper to prevent the wing from deforming beyond the baseline configuration shape (curve upward) when the aerodynamic load is applied. Figure 3-10 illustrates the actuation scheme of the variable camber wing, Figure 3-11 shows the entire assembly of the wing structure.

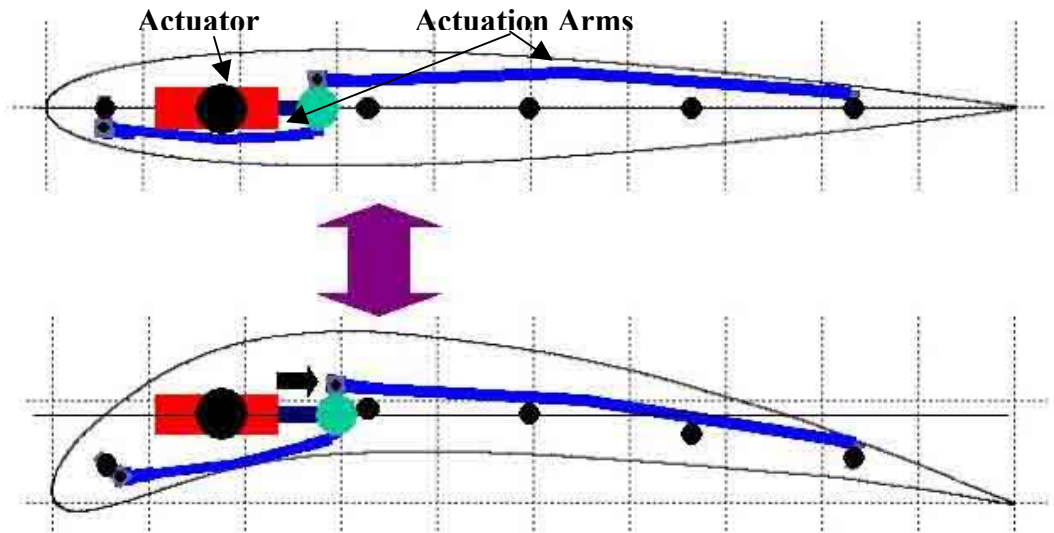


Figure 3-10 Actuation Scheme

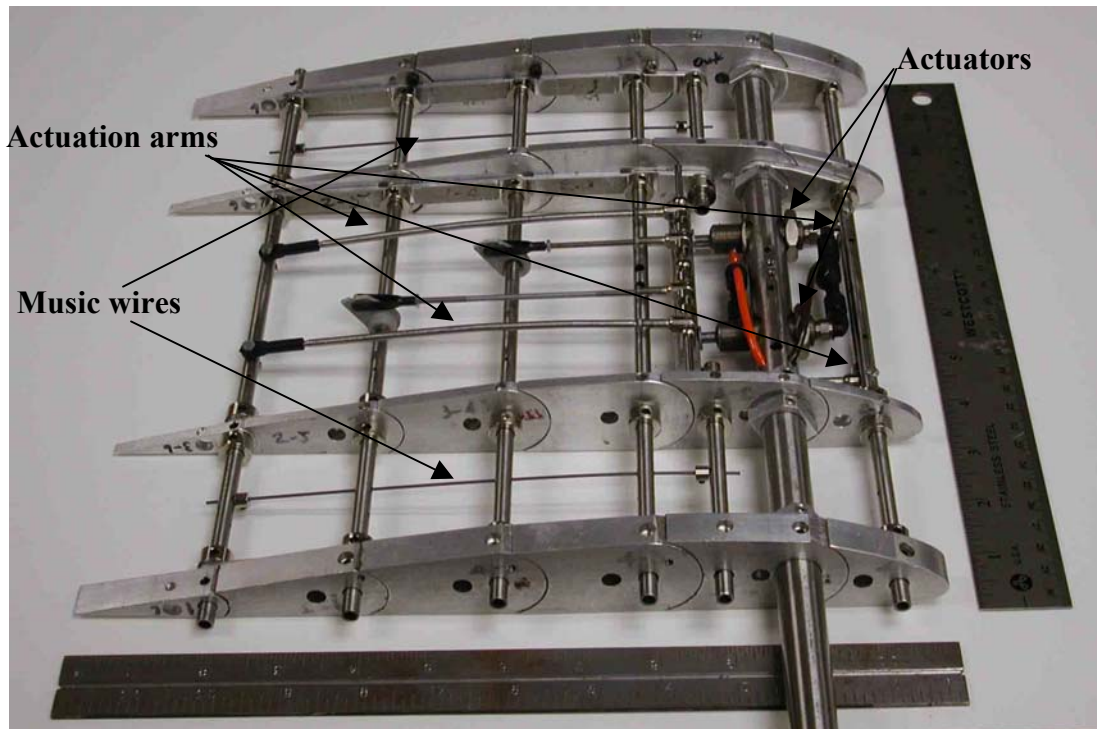


Figure 3-11 Wing structures Assembly

### 3.2.4 Wing Skin

The materials used for covering the wing model were insignia cloth, an adhesive backed polyester fabric used for banners and flags, and latex sheet. The insignia cloth is a very light, smooth, and windproof material. It has an adhesive back which conveniently allows attachment of this material onto to the wing structures. A layer of Latex sheet is first glued onto the wing ribs covering both top and bottom surface of the wing then strips of 1-inch and 1.25-inch insignia cloth and latex are glued on top of the layer of latex sheet to re-enforce the strength. The area on the rib where two rib sections meet is covered with the latex strip only because this area change its size when the wing is cambered so the elastic covered for this area is required. The strips of insignia cloth are glued on the wing surface anywhere else away from the joint of rib sections. Figure 3-12 shows the wing with skin material; latex sheet is white and insignia cloth is black.

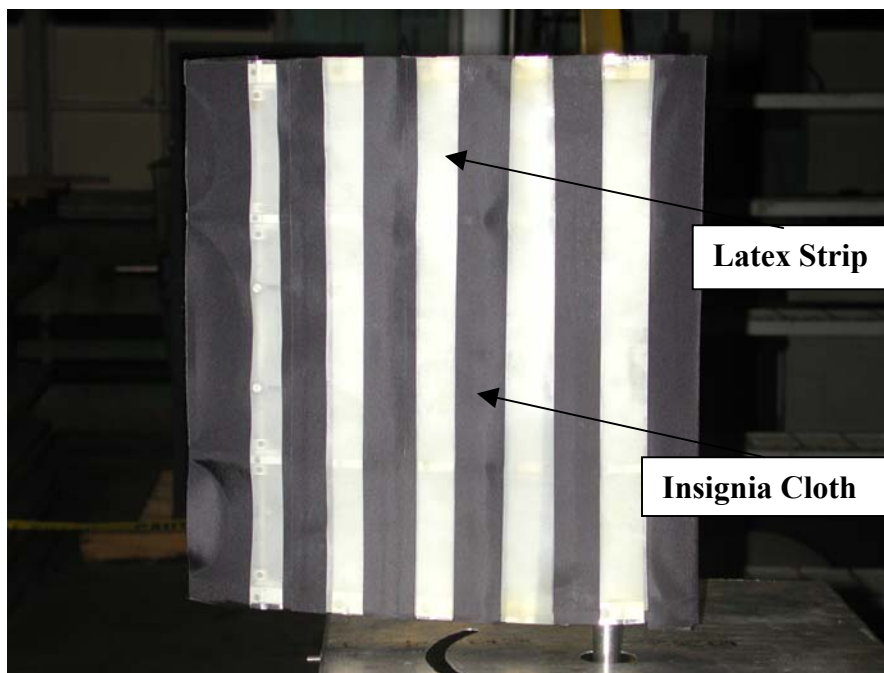


Figure 3-12 Wing with Skin

### 3.3 Rigid Wing Models

Two rigid wing models for the baseline configuration and for the cambered configuration were constructed to compare the test results with those of the variable camber wing. The shape of the cambered configuration is obtained from the contour trace of the variable camber wing before the skin was applied onto it.

Both rigid wings were made of hot-wired Styrofoam core wrapped with 2 layers of fiberglass and cured in the oven at 185 degrees for 12 hours. After curing, the surfaces of both wings were sanded to reduce skin friction drag. The rigid wings had the same span and chord length as the variable camber wing. The wing spars were also installed at the 1/6 of the chord as in the variable wing. The baseline configuration wing was based on the NACA0012 airfoil whereas the cambered configuration was based on the customized airfoil obtained from contour drawings using Xfoil software.<sup>37</sup> Figure 3-13 and figure 3-14 show the cross-section view of the baseline configuration and camber configuration rigid wing respectively.



**Figure 3-13 Baseline Rigid Wing**



**Figure 3-14 Cambered Rigid Wing**

Detailed descriptions of both variable camber wing and the rigid wing models were discussed in this chapter. This wing models will be used as an object in computing the aerodynamic results using equations provided in the next chapter.

## 4 AERODYNAMIC ANALYSIS

The focus of this research was to explore the possibility of using a multi-section variable camber wing concept to enhance the range and endurance of Unmanned Aerial Vehicles (UAVs). Therefore, the low-speed (less than Mach 0.6) aerodynamics was investigated. The influence of a variable camber wing on the ability of a UVA to fly further and longer is shown below in the general Range and Endurance equations for propeller-driven aircraft. The method used to estimate the theoretical lift and drag for the wing models is also presented in this chapter.

### 4.1 Aircraft Range and Endurance

Range, by definition, is the total distance (measured with respect to the ground) traversed by an airplane on a single load of fuel.<sup>38</sup> The general Range equation is

$$R = \int_{W_1}^{W_0} \frac{V_\infty}{c_t} \frac{L}{D} \frac{dW}{W} \quad (1)$$

One can see that in order to obtain the largest range, the aircraft needs to be flying at the highest possible velocity at the highest possible L/D, to have the smallest lowest possible specific fuel consumption, and to carry a large amount of fuel. Since the specific fuel consumption of an aircraft is dependent on the engine type, and the amount of fuel carried is limited by the size of the fuel storage, and because of the value of L/D of the aircraft varies with the angle of attack which in turn changes as  $V_\infty$  changes in level flight, the strategy of obtaining the highest flight range for a given aircraft is therefore to fly the airplane such that the product of  $V_\infty L/D$  is maximized. For a propeller-driven airplane, which is used as propulsion system for most UAV's, assuming constant velocity, specific fuel consumption, and lift to drag ratio, the range equation can be written as:

$$R = \frac{V_\infty}{c_i} \frac{L}{D} \ln \frac{W_0}{W_1} \quad (2)$$

For a propeller driven airplane,

$$c_i = \frac{c V_\infty}{\eta_{pr}} \quad (3)$$

Thus the range equation can be rewritten as

$$R = \frac{\eta_{pr}}{c} \frac{L}{D} \ln \frac{W_0}{W_1} \quad (4)$$

As one can see, one way to obtain the maximum range is to fly the plane at maximum L/D which can be achieved by altering the wing shape in different flight regimes using a variable camber wing.

Endurance is the amount of time that an airplane can stay in the air on a single load of fuel.<sup>38</sup> The general equation for endurance of aircraft is

$$E = \int_{W_1}^{W_0} \frac{1}{c_t} \frac{L}{D} \frac{dW_f}{W} \quad (5)$$

Although the general equation for endurance is very similar to the general range equation, the flight conditions for maximum endurance are different from those for maximum range, for different types of propulsion systems. For propeller-driven aircraft, the specific fuel consumption is given in term of the relation between  $c$  and  $c_t$  as shown in equation (3); thus the endurance equation can be re-written as

$$E = \int_{W_1}^{W_0} \frac{\eta_{pr}}{c} \frac{C_L}{V_\infty C_D} \frac{dW_f}{W} \quad (6)$$

The expression for lift is  $L = W = \frac{1}{2} \rho_\infty V_\infty^2 S C_L$  (7)

therefore  $V_\infty = \sqrt{\frac{2W}{\rho_\infty S C_L}}$  (8)

Equation (6) can then be rewritten as

$$E = \int_{W_1}^{W_0} \frac{\eta_{pr}}{c} \sqrt{\frac{\rho_\infty S C_L}{2W}} \frac{C_L}{C_D} \frac{dW_f}{W} \quad \text{or} \quad E = \int_{W_1}^{W_0} \frac{\eta_{pr}}{c} \sqrt{\frac{\rho_\infty S}{2}} \frac{C_L^{3/2}}{C_D} \frac{dW_f}{W^{3/2}} \quad (9)$$

From equation (9), one way to maximize the endurance of the propeller driven airplane is to fly the plane at maximum  $\frac{C_L^{3/2}}{C_D}$ . As for the range problem, a variable camber wing is needed to meet the requirement of achieving maximum endurance.

## 4.2 Development of the Estimated Lift and Drag Coefficient of the Variable Camber Wing

The theoretical estimation of lift and drag of the wing is done using NACA0012 airfoil data for the baseline configuration, and NACA9312 airfoil data for the cambered configuration. Figure 4-1 shows the cross-sections of the actual model in the cambered configuration and the NACA9312.

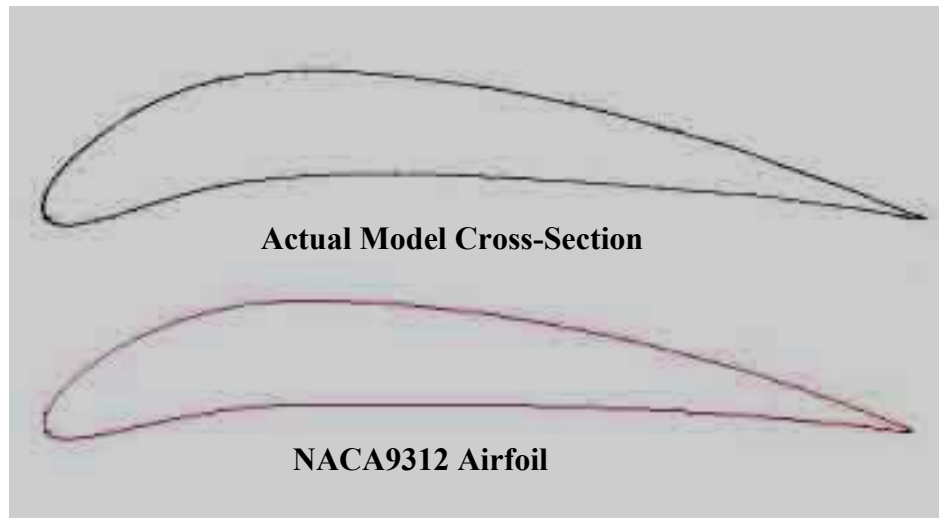


**Figure 4-1 Cross-Section Drawing of Model Wing in Cambered Configuration and NACA9312**

The computations for lift and drag coefficients of the variable camber wing for both baseline and camber configurations were performed as follows:

### 4.2.1 Lift Calculation

The lift coefficient for a low-speed wing is expressed as:

$$C_L = a(\alpha - \alpha_{L=0}) \quad (10)$$

where  $a$  is the lift curve slope. For a low-aspect-ratio straight wing in an incompressible flow, the approximation of this value was obtained by Helmbold in Germany in 1942.

Based on a lifting surface solution for elliptic wings using the theoretical lift curve slope of a thin plate  $a_0$  and aspect ratio  $AR$ , Helmbold's lift curve slope equation is expressed as:<sup>40</sup>

$$a = \frac{a_0}{\sqrt{1 + [a_0 / (\pi AR)]^2} + a_0 / (\pi AR)} \quad (11)$$

where  $a_0 = 2\pi$  is the theoretical lift curve slope

For symmetric airfoils the angle of zero lift,  $\alpha_{L=0}$ , is zero. For cambered airfoils, a simple approximation of this angle can be computed using Munk's solution or using Pankhurst's solution. Munk's solution is defined as:<sup>40</sup>

$$-\alpha_0 = k_1 y_1 + k_2 y_2 + k_3 y_3 + k_4 y_4 + k_5 y_5 \quad (12)$$

where  $y_1, y_2$ , etc., are the ordinates of the mean line expressed as fraction of the chord at points  $x_1, x_2$ , etc. These mean line points and the corresponding values of constants  $k_1, k_2$ , etc. are given table A.1 in the appendix.

The approximate solution for angle of zero lift obtained by Pankhurst's solution can be written in the following form:

$$\alpha_{L=0} = \sum A(U + L) \quad (13)$$

where  $U, L$  = upper and lower ordinates of wing section in fractions of chord corresponding to mean line points

$A, B$  = Constants values corresponding to mean line points

The parameter values used to compute Pankhurst's angle of zero lift are given in table A.2 in the appendix.

#### 4.2.2 Drag Calculation

The drag of a finite wing consists of two parts: the profile drag, which consists of skin-friction drag and pressure drag due to flow separation, and the so call "induced drag," which is a pressure drag caused by the wing tip vortices. Thus the drag coefficient of the finite wing can be expressed as:

$$C_D = c_d + C_{D_i} \quad (14)$$

where  $c_d = c_{d_f} + c_{d_p}$  is the profile drag and  $C_{D_i}$  is the induced drag

The theoretical drag coefficient used in this research was computed using the Xfoil software,<sup>41</sup> which obtained  $c_d$  by applying the Squire-Young formula at the last point in the wake. The equation for  $c_d$  is defined as:

$$c_d = D / q_\infty = 2\theta_\infty = 2\theta(u/V)^{(H+5)/2} \quad (15)$$

where  $\theta$  = momentum thickness at the end of computed wake

$u$  = edge velocity at the end of computed wake

$H$  = shape parameter at the end of computed wake

$\theta_\infty$  = momentum thickness very far downstream

$V$  = freestream velocity very far downstream

The Squire-Young formula extrapolates the momentum thickness to downstream infinity. It assumes that the wake behaves in an asymptotic manner downstream of the point of application. This assumption is strongly violated in the near-wake behind an airfoil with trailing edge separation, but is always reasonable some distance behind the airfoil.<sup>41</sup>

In the Xfoil code, the profile drag is calculated by itself and not by combining skin friction drag and pressure drag together. The friction drag coefficient is calculated by the integration of the skin friction coefficient defined with respect to the freestream dynamic pressure, and not the boundary layer edge dynamic pressure as in boundary layer theory.<sup>36</sup> This calculation can be expressed as:

$$c_{d_f} = \oint c_f d\bar{x} \quad (16)$$

The pressure drag is then deduced from the profile drag and skin friction drag instead of being calculated via pressure integration as:

$$c_{d_p} = \oint c_p d\bar{y} \quad (17)$$

The induced drag is caused by the wing tip vortices which generate an induced perturbing flow field over the wing, which in turn perturbs the pressure distribution over the wing surface in such a way that the integrated pressure distribution yields an increase in drag.<sup>31</sup> The induced drag is calculated as

$$C_{D_i} = \frac{C_L^2}{\pi e AR} \quad (18)$$

where  $e$  is the span efficiency factor. It is a function of the wing's aspect ratio and taper ratio and usually varies between 0.95 and 1.0.

One can see that as the wing camber increases, the lift of the wing increases, but this causes the induced drag to increase as well. Therefore the trade-off of a cambered wing is the higher induced drag. Increasing the aspect ratio of the wing will help by improving the performance of a variable camber wing.

The ability to alter the lift-to-drag ratio of an airplane wing plays an important role in increasing the range and endurance of the airplane as shown above. The method for approximating lift and drag is also shown. The theoretical values of lift and drag obtained using this process are compared with the actual wind tunnel test results in the next chapter.

## **5 EXPERIMENTAL TESTING OF A MULTI-SECTION VARIABLE CAMBER WING**

The purpose of this research is to investigate the aerodynamic properties of a multi-section variable camber wing. As stated in the previous chapter, two rigid wings, one for baseline configuration and one for cambered configuration were made to compare experimental results with the variable camber wing. Only lift and drag were obtained from the wind tunnel testing because the test balance was not equipped with moment sensor. The test apparatus, procedure, and results are shown in the following sections.

### **5.1 Experimental Test Apparatus**

#### **5.1.1 Wind Tunnel**

The “free-jet” wind tunnel (shown in figure 5-1) designed and built by Dr. Allen Winkelmann, Aerospace Engineering professor at the University of Maryland, was used to test the wing models. It has a test section of 22-by-22 in. with a contraction ratio of 0.13 and a turbulence level of 0.25%. The operational speeds of the wind tunnel are 35-115 ft/s and were controlled by a variac. A manometer and pitot probe were used to measure the airspeed.

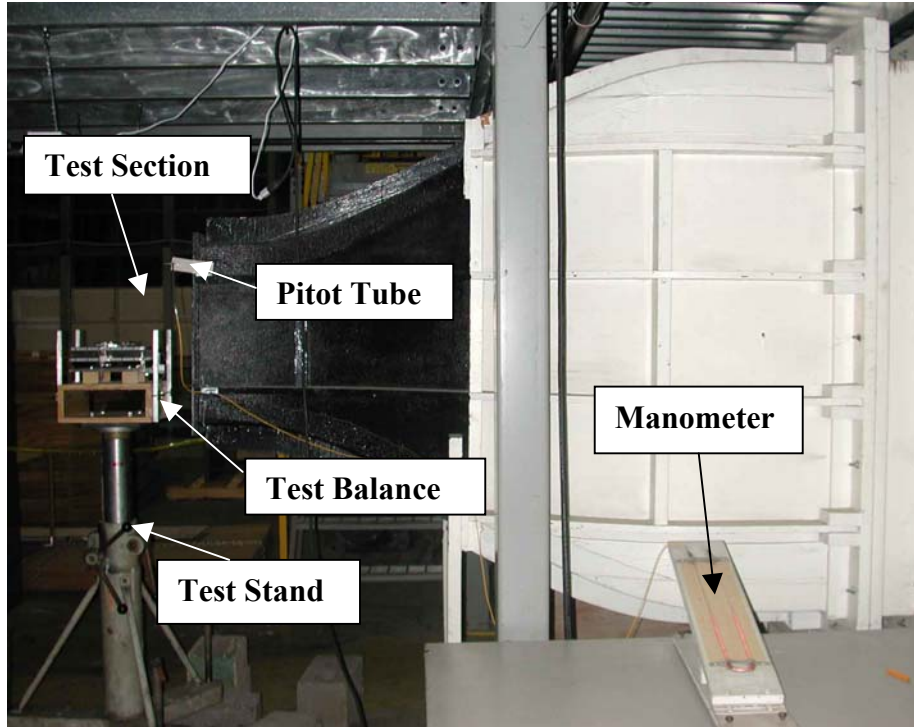


Figure 5-1 Free-Jet Wind Tunnel

### 5.1.2 Test Balance

The test balance, shown in figure 5-2, is a rectangular-shape box with two sets of strain gaged flexures that are capable of measuring lift and drag. These two load-cells are located at the front and on one side of the box. Aluminum sheets are used as flexures for the balance. The balance has a 5/8-inch hole in the middle to secure the wing spar during the test and has a dial for measuring the angle of attack placed around this hole. Lift and drag forces on the balance are transduced into voltages, and they are displayed using two multimeters. These values are then converted into forces by using the factors obtained from calibration of the load-cells described in the next section. Two 2311 signal-conditioning units are used to provide the excitation for the load-cells and to amplify the

return signal to the multimeters. The excitation on both units was set at 5 volts and the signal gain was 100.

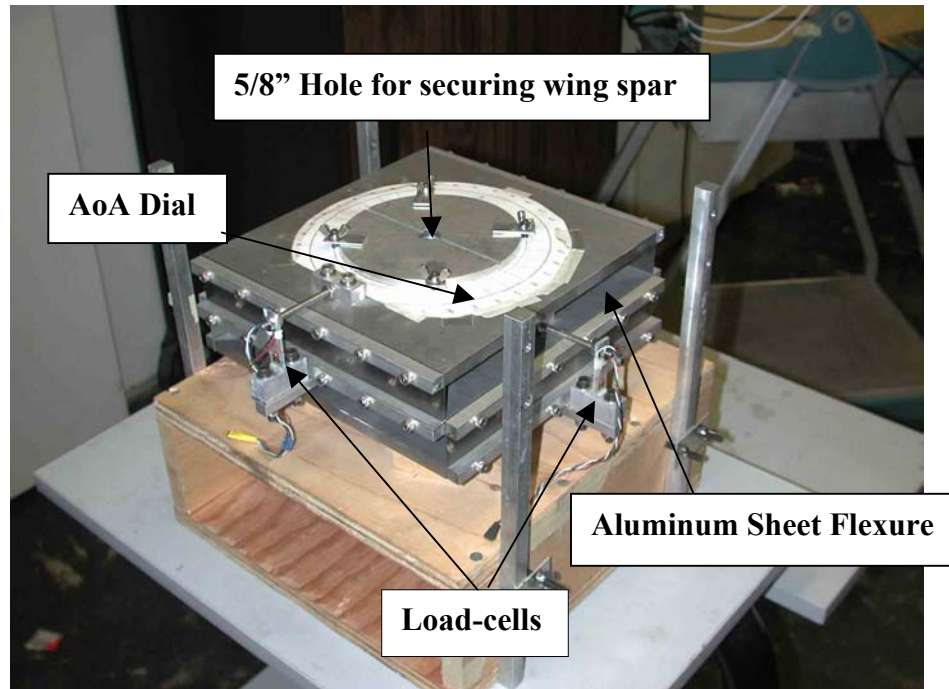


Figure 5-2 Wind Tunnel Test Balance

### 5.1.3 Load-cells Calibration

The calibration of the load-cells was done by first placing the test balance on a flat surface and tightly securing a wing spar to it. The spar was then loaded with a known weight through a string and pulley in the directions corresponding to wing lift and drag. The calibration setup is shown in figure 5-3. The voltage from the multimeter readouts was recorded for each increment and decrement of the weight mass. The loading and unloading of the weight masses were conducted 3 times each for the lift and drag directions to assure the consistency of the balance. The results were averaged and the

final conversion factors for lift and drag were obtained. Figure 5-4 and figure 5-5 show the calibration results for lift and drag respectively.

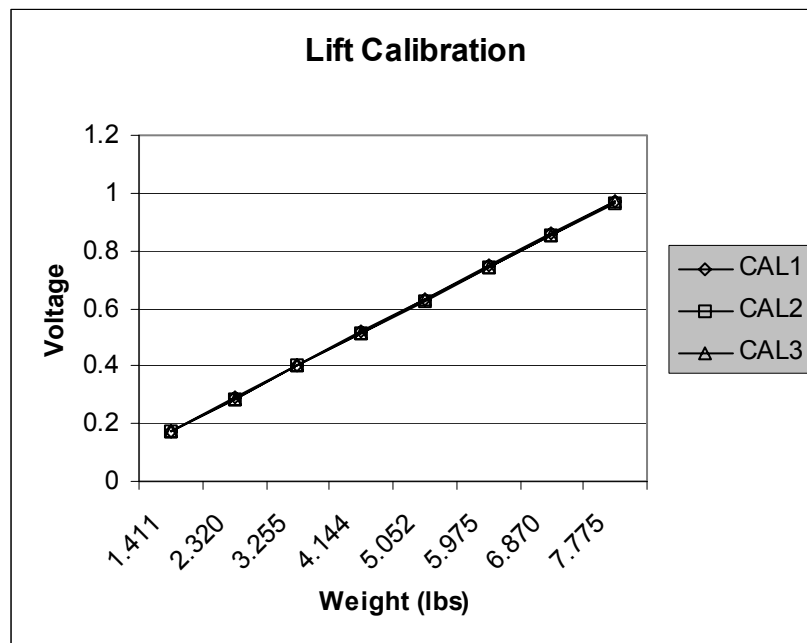
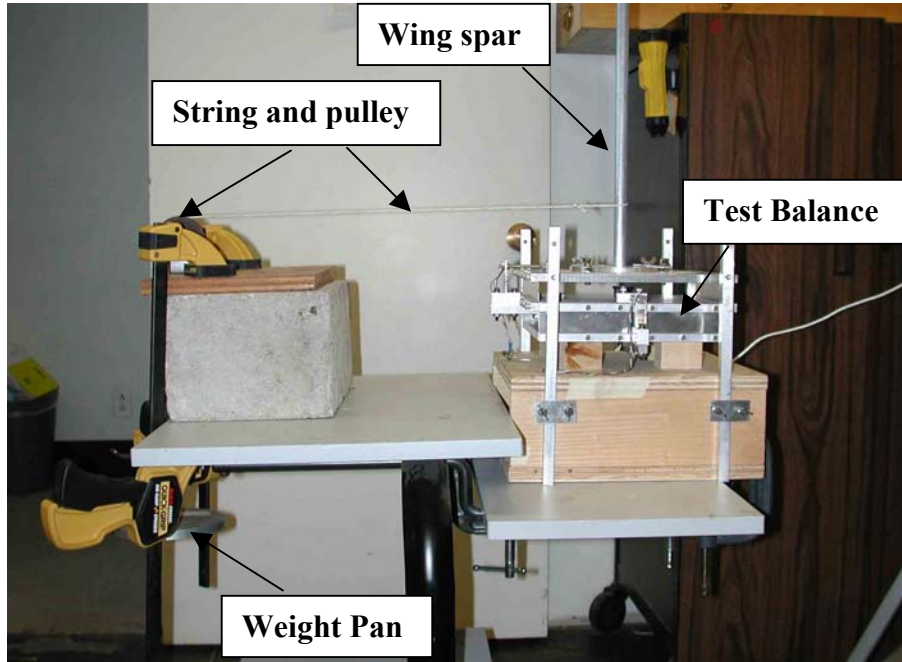


Figure 5-4 Lift Calibration Result

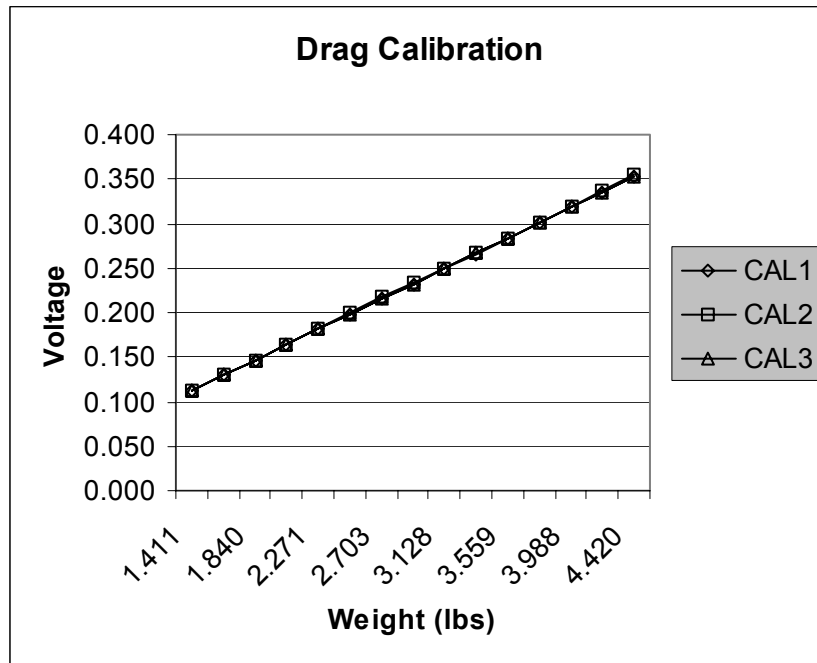


Figure 5-5 Drag Calibration Result

## 5.2 Test Matrix and Test Procedure

Both of the rigid wings and the variable camber wing were tested at the same conditions. Only static tests were performed on these three wing models. The test matrix is shown in table 5-1.

Wing Model	Airspeed (ft/s)	Angle of Attack (degree)
Rigid wing - baseline configuration	50, 75, 100	0 to 2-4 degrees after stall
Rigid wing - cambered configuration	50, 75, 100	0 to 2-4 degrees after stall
Variable camber wing - baseline configuration	50, 75, 100	0 to 2-4 degrees after stall
Variable camber wing - cambered configuration	50, 75, 100	0 to 2-4 degrees after stall

Table 5-1 Wind Tunnel Test Matrix

As displayed above, the wing model tests were performed in atmospheric conditions, at three different airspeeds: 50 ft/s, 75 ft/s, 100 with the corresponding Reynolds numbers 322000, 480000, and 636000 respectively. Lift and drag were measured from a zero degree angle of attack up to 2-4 degrees above the stall angle, since baseline configuration and cambered configuration had different stall angles.

The variable camber wing was actuated by a portable air compressor at 80 psi through a set of pressure valves as mentioned in chapter 3; two of these valves were opened to keep the wing in baseline configuration, and the other two were opened to keep the wing in cambered configuration. Even though the valves can operate up to 105 psi as stated by the manufacturer, only 80 psi of pressure was applied because higher pressures caused the air to leak between the valves and tube fittings. A 10-volts signal was generated by a Signal generator to control the opening and closing of these valves through a 2-way switch.

The rigid wing model in baseline configuration, rigid wing model in cambered configuration, the variable camber wing in baseline configuration, and the variable camber wing in cambered configuration were tested in the wind tunnel successively. At each angle of attack, each wing was tested at airspeeds of 50, 75, and 100 ft/s in that order. Once all three airspeeds were applied, the wind tunnel speed was brought down to the minimum so that the next angle of attack could be set. The change of angle of attack during test was performed manually by loosening the nut holding the main spar to the test balance then rotating the spar to the desired angle of attack. The process was repeated for each wing until the angle of attack reached 2-4 degrees beyond the stall angle.

### 5.3 Test Results

Figures 5-6 through 5-17 display lift and drag coefficients measured on the baseline and cambered wings as well as the theoretical lift and drag coefficients. Lift comparison between baseline rigid wing, baseline configuration of the variable camber wing and the theoretical lift are illustrated in figures 5-6 through 5-8. One can see that the lift coefficients of the variable camber wing are slightly higher than those of rigid wing and theoretical values. The maximum lift of the variable camber wing slightly decreases where the stall angle remains the same as Reynolds number increases. The maximum lift and stall angle of the rigid wing increase as Reynolds number increases. The experimental values of lift are higher than the theoretical values for all Reynolds numbers and for angles of attack up to stall.

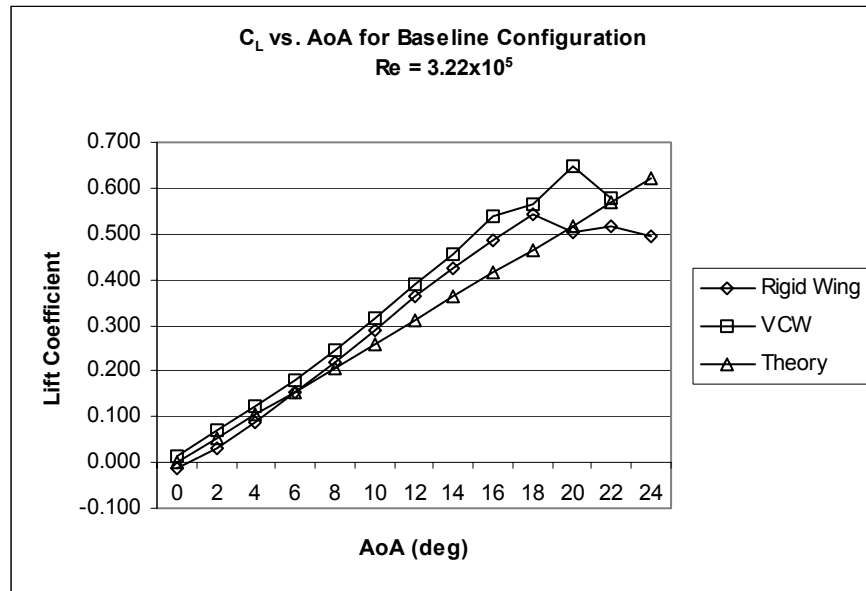
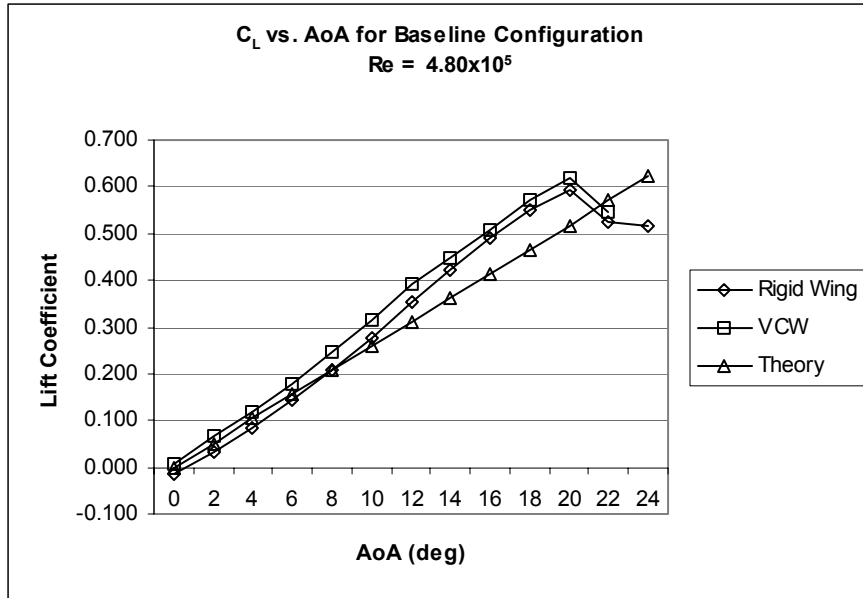
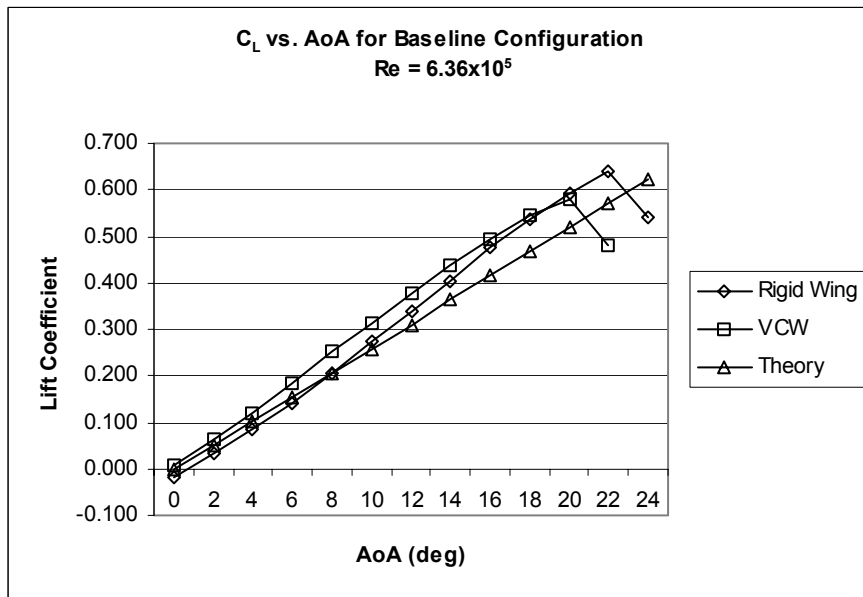


Figure 5-6 Lift Coefficient for Baseline Configuration at  $Re = 3.2 \times 10^5$



**Figure 5-7 Lift Coefficient for Baseline Configuration at Re = 4.8x10<sup>5</sup>**



**Figure 5-8 Lift Coefficient for Baseline Configuration at Re = 6.3x10<sup>5</sup>**

Figures 5-9 through 5-11 display the lift coefficient for the cambered rigid wing and the cambered configuration of the variable camber wing. One can see that the lift produced by the variable camber wing is greater than that of the rigid wing for all angles of attack. Furthermore, the variable camber wing has a stall angle more than twice as high as that of the rigid wing; the rigid wing stalls at 14 degrees angle of attack, the variable camber wing in cambered configuration stalls at 38 degrees. This is a very interesting phenomenon and will be discussed later in this chapter. As compared the theoretical lift coefficients, the variable camber wing produces slightly higher lift at high angles of attack for low Reynolds numbers but slightly lower lift at low angles of attack. The lift coefficients of variable camber wing become smaller than the theoretical values as Reynolds numbers increase. The rigid wing produces lower lift coefficients than the theoretical values for all angles of attack.

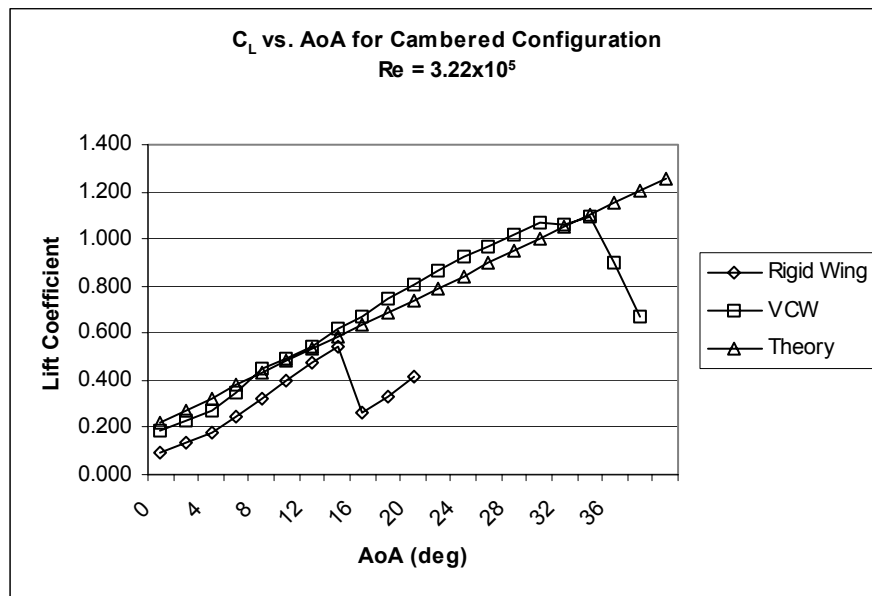


Figure 5-9 Lift Coefficient for Cambered Configuration at  $Re = 3.2 \times 10^5$

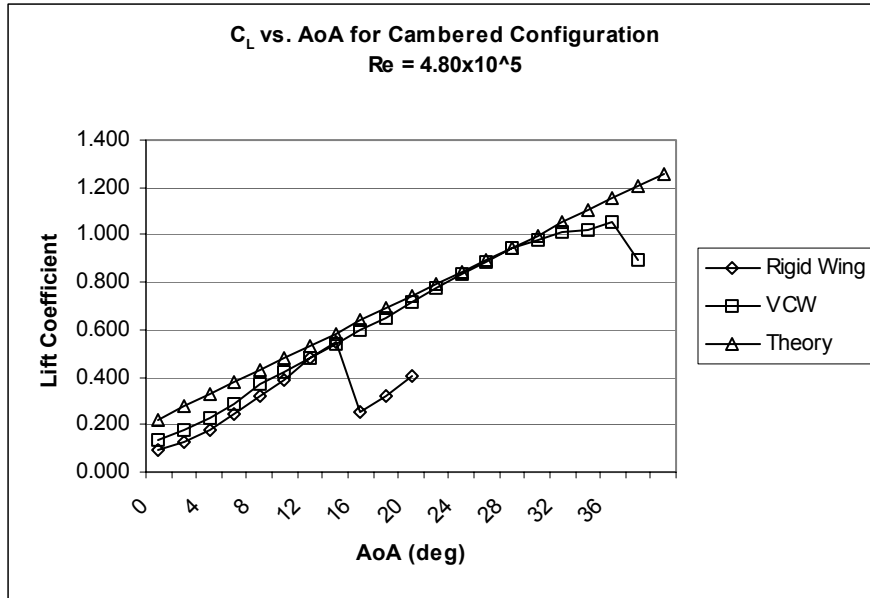


Figure 5-10 Lift Coefficient for Cambered Configuration at  $Re = 4.8 \times 10^5$

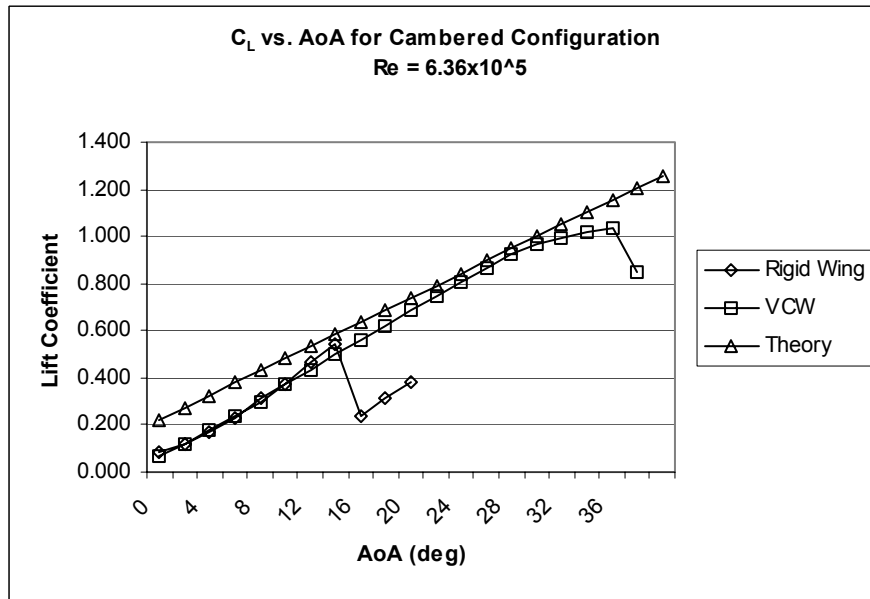


Figure 5-11 Lift Coefficient for Cambered Configuration at  $Re = 6.3 \times 10^5$

Figures 5-12 through 5-14 show the drag coefficients of the baseline rigid wing, the baseline configuration of the variable camber wing, and the theoretical values for the baseline airfoil obtained from the Xfoil software. Drag produced by variable camber wing is greater than that of the rigid wing and the difference increases as the Reynolds number increases. The theoretical drag coefficients are lower than the values obtained from the experimental results but close to that of the baseline rigid wing.

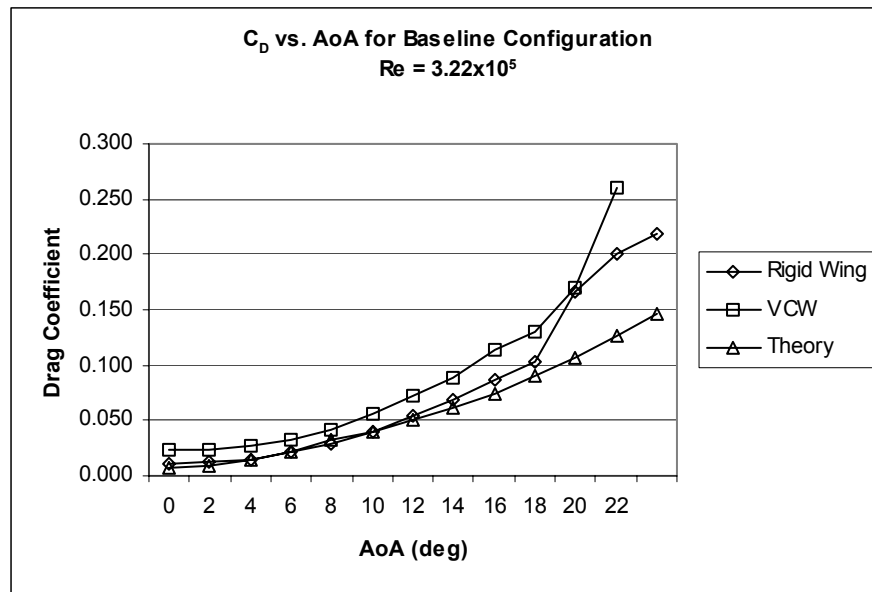


Figure 5-12 Drag Coefficient for Baseline Configuration at  $Re = 3.2 \times 10^5$

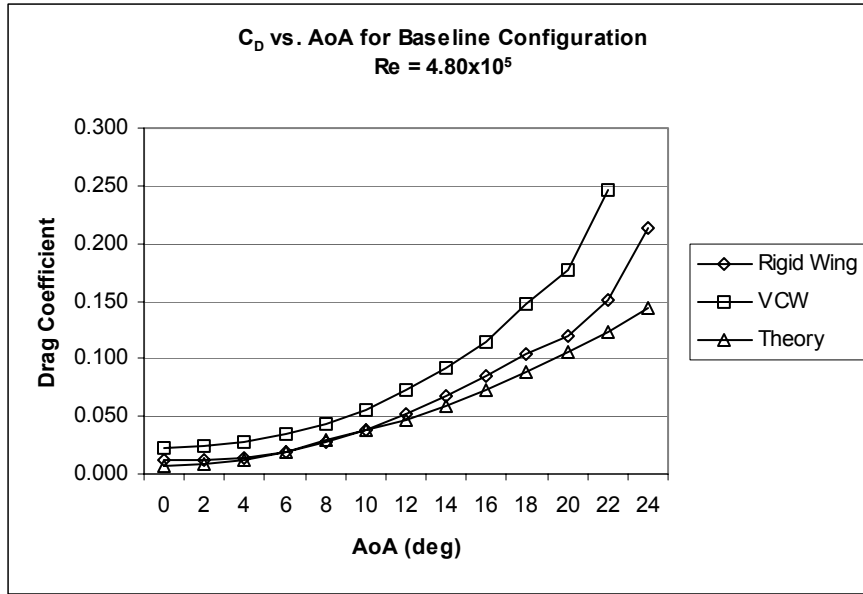


Figure 5-13 Drag Coefficient for Baseline Configuration at  $Re = 4.8 \times 10^5$

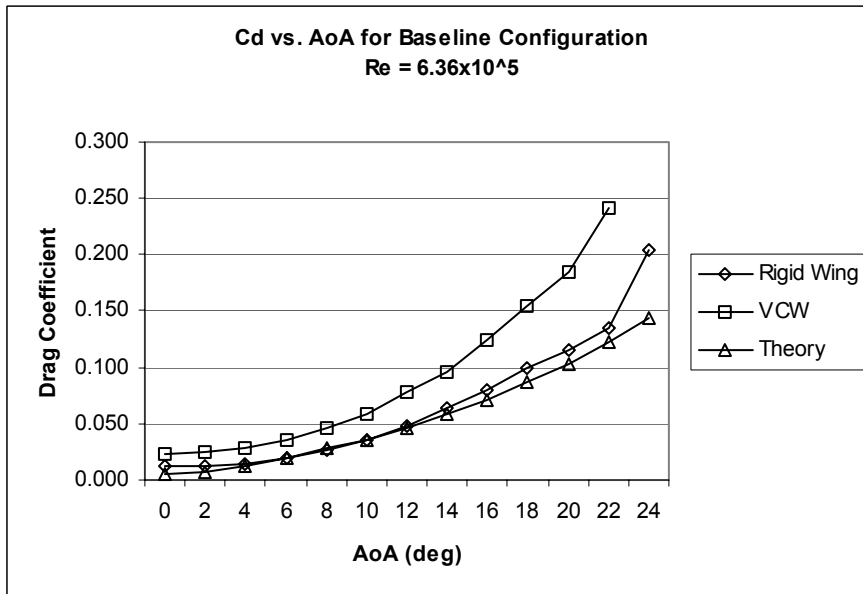


Figure 5-14 Drag Coefficient for Baseline Configuration at  $Re = 6.3 \times 10^5$

Figures 5-15 through 5-17 display the drag coefficients of the cambered rigid wing, the cambered configuration of the variable camber wing, and the theoretical values obtained for cambered configuration airfoil using Xfoil program. One can see that the drag produced by variable camber wing is less than that of the rigid wing up to the angle of attack where the cambered rigid wing stalls. The difference between the variable camber wing and cambered rigid wing also increases as the Reynolds number increases just like the baseline case, only opposite. The drag coefficients obtained from Xfoil are close to the values obtained from variable camber wing and slightly higher as Reynolds number increases.

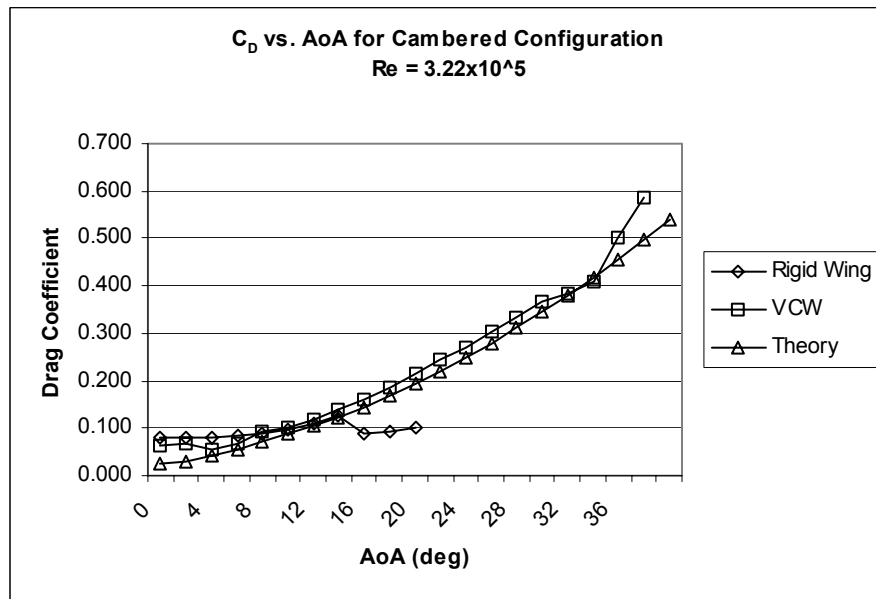


Figure 5-15 Drag Coefficient for Cambered Configuration at  $Re = 3.2 \times 10^5$

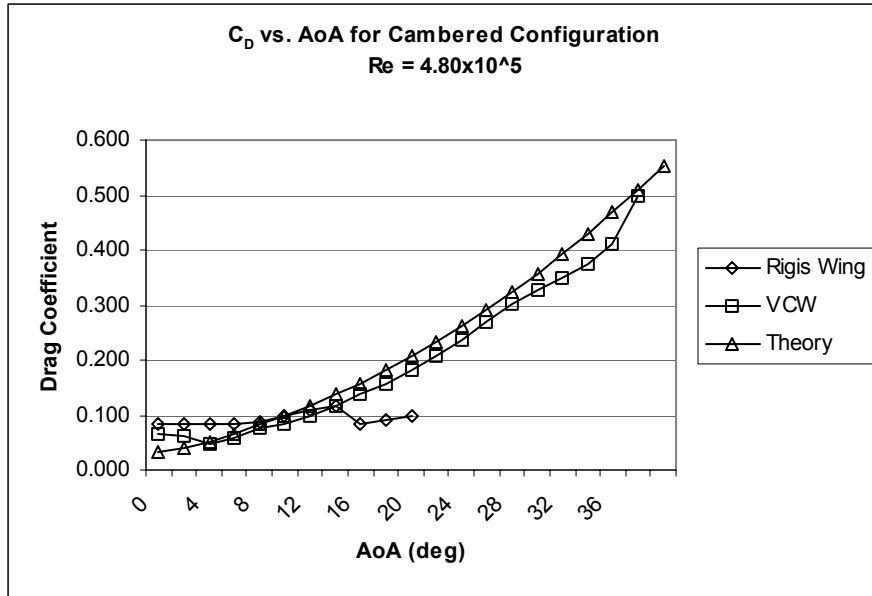


Figure 5-16 Drag Coefficient for Cambered Configuration at  $Re = 4.8 \times 10^5$

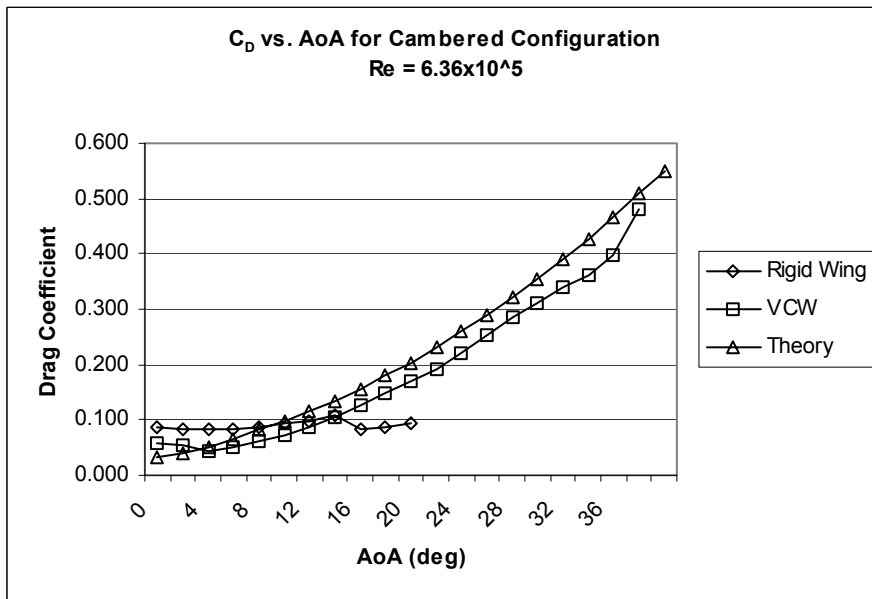


Figure 5-17 Drag Coefficient for Cambered Configuration at  $Re = 6.3 \times 10^5$

Figures 5-18 through 5-20 display the lift-to-drag ratios of the baseline rigid wing, the baseline configuration of the variable camber wing, and the theoretical values obtained from Xfoil for the baseline configuration airfoil (NACA0012). Lift-to-drag of the variable camber wing is greater than that of the rigid wing at low angle of attack, however, the lift-to-drag of the rigid wing becomes greater than that of the variable camber wing as angle of attack increases. The calculated lift-to-drag is higher than those of rigid wing and variable camber wing at low angle of attack. These calculated values fall in between those obtained from the rigid wing and the variable camber wing as angle of attack increases. The maximum lift-to-drag of the rigid wing increases slightly (from 7.5 to 8.0) as the Reynolds number increases whereas maximum lift-to-drag of the variable camber wing remains the same at 5.7. The maximum value of theoretical lift-to-drag increases from 7.5 to 8.6 as the Reynolds number increases.

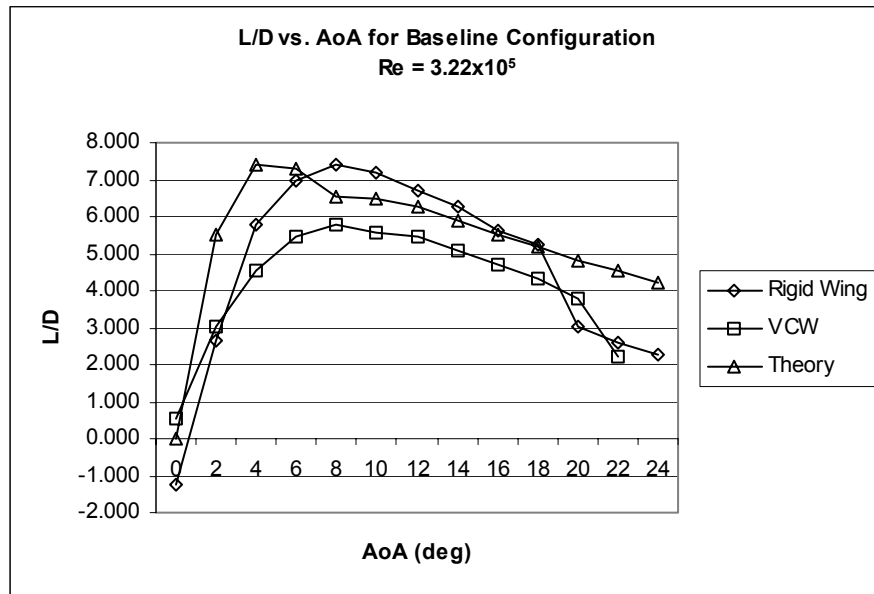


Figure 5-18 Lift-to-Drag Ratio for Baseline Configuration at  $Re = 3.2 \times 10^5$

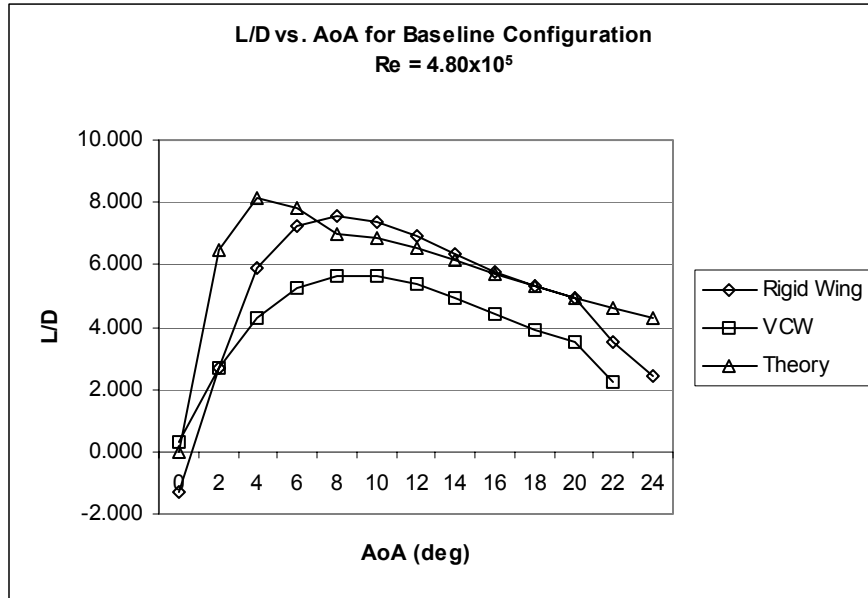


Figure 5-19 Lift-to-Drag Ratio for Baseline Configuration at  $Re = 4.8 \times 10^5$

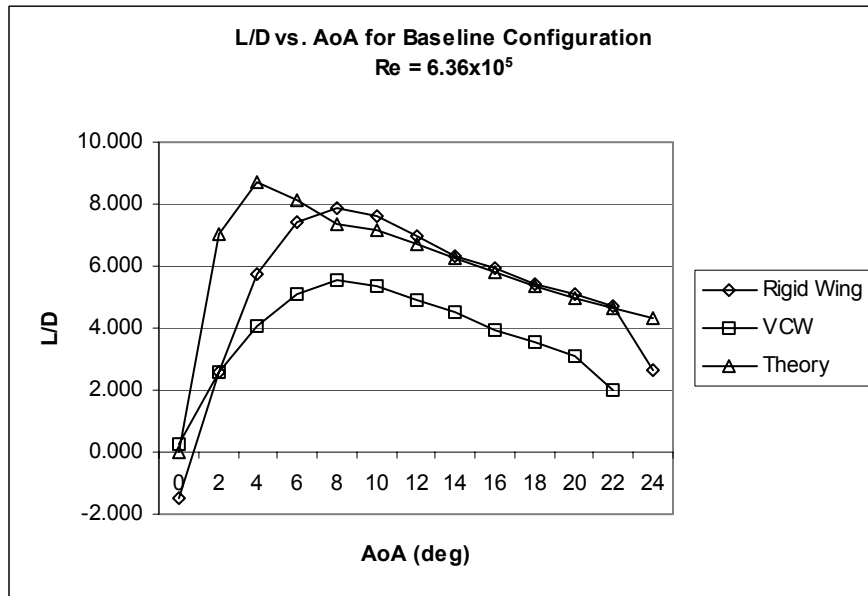


Figure 5-20 Lift-to-Drag Ratio for Baseline Configuration at  $Re = 6.3 \times 10^5$

Figures 5-21 through 5-23 illustrate the lift-to-drag ratio of the cambered rigid wing, the variable camber wing in the cambered configuration, and the values of lift-to-drag ratio of the camber configuration airfoil obtained theoretically. The lift-to-drag ratio for the variable camber wing is greater than that of the rigid wing for all three Reynolds numbers; however, these values of lift-to-drag from the variable camber wing are smaller than the theoretical values at low angles of attack. The maximum lift-to-drag ratio obtained from the variable camber wing remains the same as the Reynolds number increases whereas the lift-to-drag ratio obtained from the rigid wing and the ones obtained from the theoretical calculations increase slightly. The maximum lift-to-drag ratio obtained from the cambered configuration of the variable camber wings and theory are less than those obtained from the rigid wing.

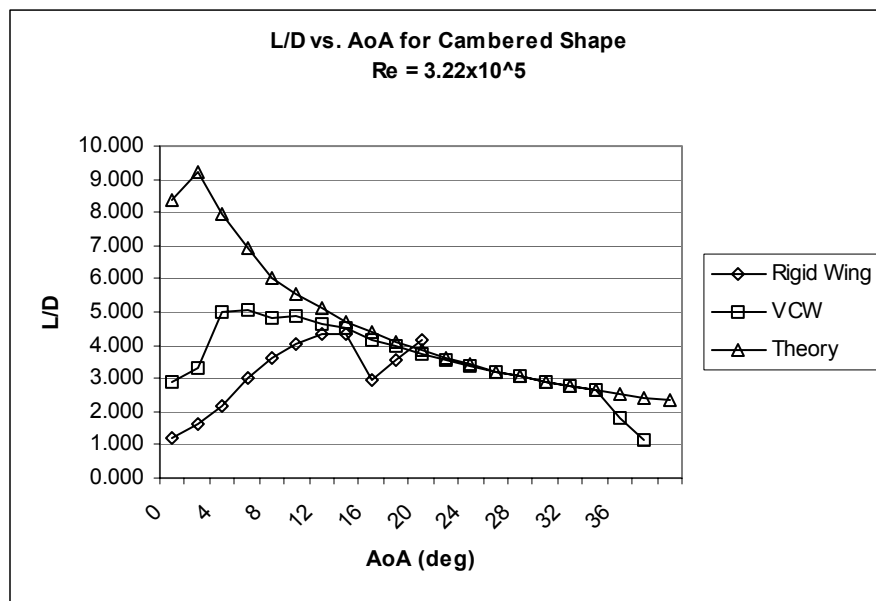


Figure 5-21 Lift-to-Drag Ratio for Cambered Configuration at  $Re = 3.2 \times 10^5$

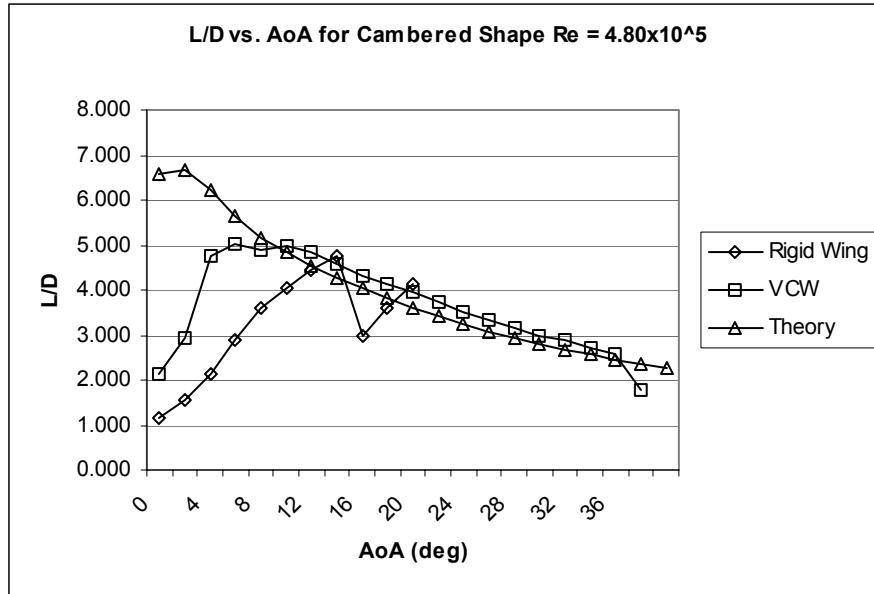


Figure 5-22 Lift-to-Drag Ratio for Cambered Configuration at  $Re = 4.8 \times 10^5$

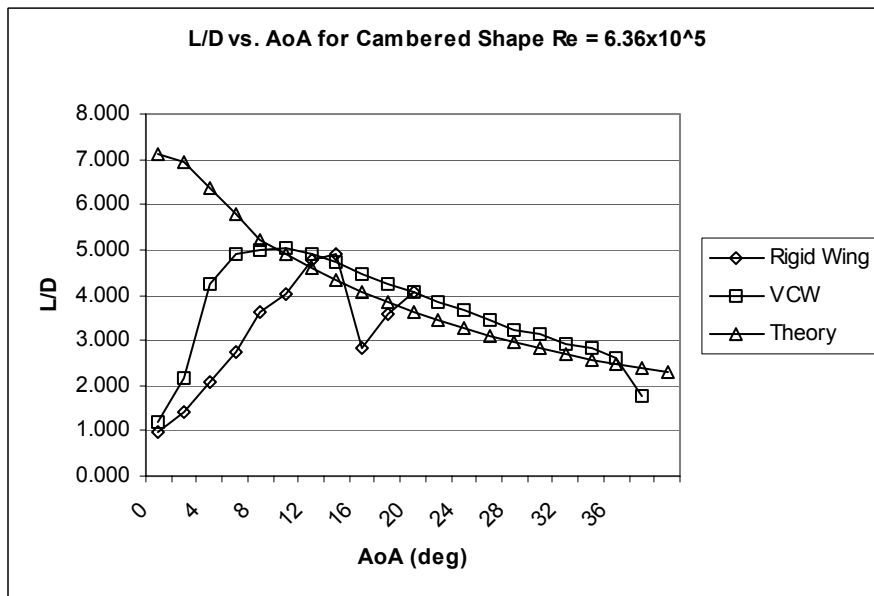
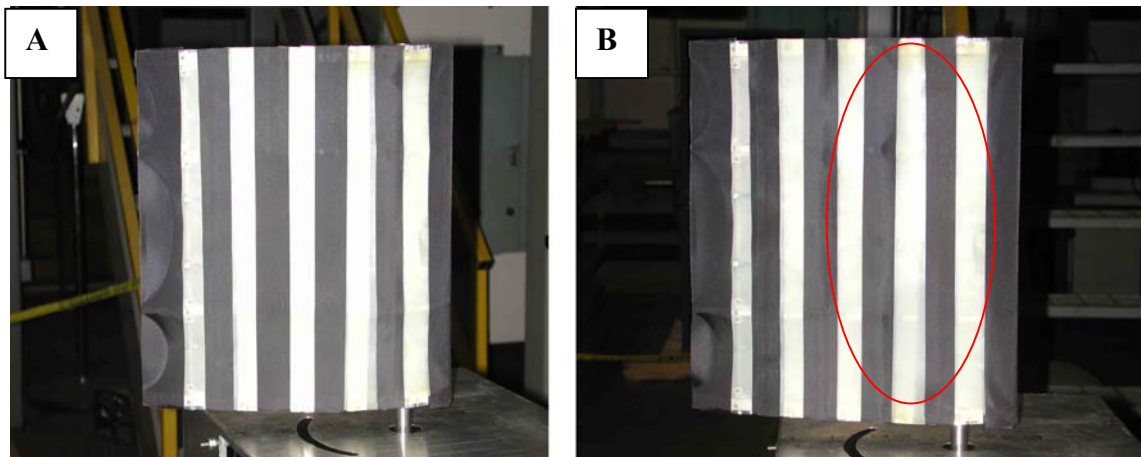


Figure 5-23 Lift-to-Drag Ratio for Cambered Configuration at  $Re = 6.3 \times 10^5$

## 5.4 Discussion of Results

As seen in the previous section, lift derived from the variable camber wing is higher than that of the rigid wing. This is possibly due to the vibration of the wing skin that keeps the flow attached to the wing and the bulge produced on the top surface as shown in figure 5-24. The vibration occurs at the latex strip at the forward portion of the wing near the main spar since it is not glued directly to the wing ribs. The low-pressure distribution at the forward portion about a quarter chord causes the skin to bulge outward on top surface of the wing creating additional camber for the variable camber wing. This bulge increased the thickness and camber of the variable camber wing.



**Figure 5-24 Wing Comparison A) No bulge on surface at 0 airspeed B) Bulge shown on top surface at 75 ft/s airspeed**

In the cambered configuration, a very high stall angle is achieved by the variable camber wing for three possible reasons: First, because of the vibration of the wing skin, the flow stays attached to the wing at high angles of attack; Second, as the wing was pitched upward, the aerodynamic force acting on the trailing edge section of the wing

slightly overcomes the force produced by the actuators which causes the trailing edge section to slightly pitch upward causing a streamline shape on the airfoil cross-section allowing flow to stay attached to the wing; And third, the variable camber wing had slightly less camber than the rigid wing due to the stiffness of the wing skin which reduced the final camber of the variable camber wing. As stated in chapter 3, the rigid wing was made using the cambered shape obtained from the variable camber wing in cambered configuration before the wing skin was applied. The amount of camber changed by approximately 2% after the wing was covered with the skin.

Since the skin for variable camber wing is made of layers of fabric and latex sheets glued on top of each other, high drag occurs around the seams between these materials. Therefore, the drag for variable camber wing in the baseline configuration is higher than that of the rigid wing which has its skin smoothly sanded. For the cambered configuration, the flexibility of the skin helps to reduce the drag on the variable camber wing. The wing skin on top surface of the wing becomes tighter and smoother as it is being forced to curve. The bottom surface of wing also becomes tighter do to high pressure. The theoretical drag derived from the Xfoil software is greater than those derived from the experiment because of errors in numerical accuracy. Since the cambered airfoil involves large separation bubbles, a large number of panels are needed in calculating the drag to get an accurate result. The cambered airfoil used in this research was drawn without a sufficient number of panels, therefore the drag calculated is high compared to the experimental results.

Even though variable camber wing in the baseline configuration produces higher lift than the baseline rigid wing, it produces higher drag as well. The increase in drag is in a

much higher ratio to the increase in lift causing the lift-to-drag ratio to be lower for the variable camber wing. The increase in lift and decrease in drag of the variable camber wing in cambered configuration results in a higher lift-to-drag ratio than that of cambered rigid wing. However, the values of maximum lift-to-drag ratio for cambered configuration are lower than that of baseline configuration due to higher drag values.

## 5.5 Summary of test results

Table 5-2 through table 5-4 show the summary of the test results at  $Re = 3.2 \times 10^5$ ,  $Re = 4.8 \times 10^5$ , and  $Re = 6.3 \times 10^5$ , respectively.

Parameters	Baseline rigid	Baseline VCW	Cambered rigid	Cambered VCW
Max L/D	7.4 at 8°	5.8 at 8°	4.4 at 14°	5.1 at 6°
Max $C_L$	0.54 at 18°	0.65 at 20°	0.55 at 14°	1.09 at 34°
Max $C_D$	0.22 at 24°	0.26 at 22°	0.13 at 14°	0.59 at 38°
Stall Angle	18°	20°	14°	34°

**Table 5-2 Summary of Test Results at  $Re = 3.2 \times 10^5$**

Parameters	Baseline rigid	Baseline VCW	Cambered rigid	Cambered VCW
Max L/D	7.6 at 8°	5.7 at 8°	4.7 at 14°	5.0 at 6°
Max $C_L$	0.59 at 20°	0.62 at 20°	0.55 at 14°	1.05 at 36°
Max $C_D$	0.21 at 24°	0.25 at 22°	0.12 at 14°	0.5 at 38°
Stall Angle	20°	20°	14°	36°

**Table 5-3 Summary of Test Results at  $Re = 4.8 \times 10^5$**

<b>Parameters</b>	Baseline rigid	Baseline VCW	Cambered rigid	Cambered VCW
Max L/D	7.9 at 8°	5.5 at 8°	4.9 at 14°	5.0 at 10°
Max C <sub>L</sub>	0.64 at 22°	0.58 at 20°	0.54 at 14°	1.03 at 36°
Max C <sub>D</sub>	0.20 at 24°	0.24 at 22°	0.11 at 14°	0.48 at 38°
Stall Angle	22°	20°	14°	36°

**Table 5-4 Summary of test results at  $Re = 6.3 \times 10^5$**

Even though these tables seem to show a fair comparison between the rigid wing and the variable camber wing, this comparison is not quite correct. The variable camber wing in cambered configuration out performed the stall characteristics of the rigid wing because the wing skin was segmented and acted as a pseudo-boundary layer trip. In addition, the flexibility of the variable wing skin injected the energy into the flow by vibrating. Therefore, for the comparison to be more accurate, the same type of material must be applied on the rigid wing.

## **6 CONCLUSION**

### **6.1 Conclusions**

A multi-section variable camber wing, using six rib sections with pneumatic actuators and a simple linkage system embedded inside the wing, was designed as another means to vary the shape of a wing. This variable camber wing did not involve complicated actuation components or a control system, but effectively provided satisfactory changes in wing camber. A change in camber of 10% before applying the wing skin, and 8% after applying wing skin, were obtained from this wing concept.

Three wing models, one variable camber wing and two rigid wings, of 12-in chord and 12-in span were built for wind tunnel testing. The size of the wing model was determined from the test result of other wing models previously in the same wind tunnel. The aluminum wing rib sections manufactured by CNC machine, the chain links, and the stainless steel tubes were the primary structures of the variable camber wind tunnel model. The variable camber wing was covered by the combination of latex sheet and insignia cloth which provided very satisfactory flexibility, strength and stiffness. The latex sheet showed low magnitude but high frequency vibration during testing causing the flow to attach to the wing and delay separation. This was an unexpected phenomenon which benefited the test results. Two rigid wings for the baseline and cambered

configurations of the variable camber wing were built using foam core and composite wing skin for comparison of wind tunnel test results.

The research was mostly experimental, based on wind tunnel test results. The tests were done in a free-jet wind tunnel with the open test section of 22-by-22 in. A load-cell test balance was used to measure lift and drag. The measured aerodynamic coefficients were used to determine the advantage of variable camber wing over that of a rigid wing. The wind tunnel results were also used to compare with the calculated values obtained from the Xfoil software. The static test was performed at airspeeds of 50 ft/s, 75 ft/s, and 100 ft/s or at the chord Reynolds numbers of 322000, 479000, and 636000 respectively, in the same atmosphere conditions for all three wings. The wind tunnel results showed significant advantages of the variable camber over the rigid wing in camber configuration, such as higher stall angle and higher lift-to-drag ratio. However, due to high drag generated by the wing skin of the variable camber wing during baseline configuration, the lift-to-drag ratio of the variable camber wing was lower than the baseline rigid wing.

The comparison of wing performance between the rigid wings and the variable camber wing was not quite accurate since the flexibility of the wing skin caused the vibration injecting the energy into the flow. Additionally, the wing skin of the variable camber wing acted as a pseudo-boundary layer trip keeping the flow attach to the wing.

## 6.2 Contributions

The contributions resulting from this research can be highlighted as follows:

- A variable camber wing with multi-rib sections and embedded pneumatic actuators was designed and manufactured.
- The pneumatic actuation mechanism performed well in changing the wing configuration and keeping the wing shape stable.
- Simple push-pull actuation scheme was used
- A multi-rib section concept can provide up to 10% increase in wing camber before the skin is applied and up to 8% increase after the skin is applied without major discontinuity or sudden change on the wing surface as seen in conventional high-lift devices.
- The vibration of wing skin possibly keeps the flow attached to the wing, delaying separation and resulting in high stall angle.
- The vibration of the wing skin possibly causes the lift on the variable camber wing in both configurations to be greater than that of rigid wing.
- The variable camber wing in cambered configuration had higher lift-to-drag ratio whereas the variable camber wing in baseline configuration suffered high skin friction drag caused the lift-to-drag ration to be lower than of rigid wing.

### 6.3 Future Work

There is much that can be done to improve the variable camber wing concept.

Possible future work for this research can be stated as follow:

- The wing skin was the major cause of low performance, especially the increase in drag, therefore more research should be done on obtaining better wing skin materials.
- More research should be done on the effect of wing skin vibration to validate some of the results in this research.
- Even though the pneumatic actuation system provides a very satisfactory result in alternating the wing configuration, it can only provide two values of camber. Therefore, a linear actuator or other type of actuator that can be controlled to provide intermediate configurations needs to be investigated.
- A Thin flexure could be used for connecting the rib sections together instead of the link shown in this research to reduce weight and reduce complexity.
- The test balance and test equipment should be improved to provide better and more accurate test results. The changing of angle of attack should be done automatically through gears or motor servos.
- The rigid wing in cambered configuration should be built based on the cambered configuration of variable camber wing after the wing skin is installed.
- Same type of skin material should be applied to both variable camber wing and rigid wing to provide fair comparison.

## APPENDIX

### ANGLE OF ZERO LIFT CALCULATING PARAMETERS

**Table A.1: Parameter Values for Munk's Solution**

Mean Line Ordinates	Values	Constants	Values
x <sub>1</sub>	0.99459	k <sub>1</sub>	1252.24
x <sub>2</sub>	0.87426	k <sub>2</sub>	109.048
x <sub>3</sub>	0.50000	k <sub>3</sub>	32.5959
x <sub>4</sub>	0.12574	k <sub>4</sub>	15.6838
x <sub>5</sub>	0.00542	k <sub>5</sub>	5.97817

**Table A.2: Parameter Values for Pankhurst's Solution**

Mean Line Ordinates	Constants	
x	A	B
0	1.45	-0.119
0.025	2.11	-0.156
0.05	1.56	-0.104
0.1	2.41	-0.124
0.2	2.94	-0.074
0.3	2.88	-0.009
0.4	3.13	0.045
0.5	3.67	0.101
0.6	4.69	0.170
0.7	6.72	0.273
0.8	11.75	0.477
0.9	21.72	0.786
0.95	99.85	3.026
1.0	-164.90	-4.289

## REFERENCES

1. Pern, N.J., Jacob, J.D., "Aerodynamic Flow Control Using Shape Adaptive Surfaces," Proceeding of 1999 ASME Design Engineering Technical Conferences, September 12-15, 1999. Las Vegas, Nevada, USA.
2. Munday, David, Jacob, Jamey, "Active Control of Separation on a Wing with Conformal Camber," AIAA 2001-0293.
3. Munday, David, Jacob, Jamey D., Hauser, Thomas, and Huang, George, "Experimental and Numerical Investigation of Aerodynamic Flow Control Using Oscillating Adaptive Surfaces," AIAA 2001-2837.
4. Munday, David, Jacob, Jamey, "Active Control of Separation on a Wing with Oscillating Camber," AIAA Journal of Aircraft, Vol. 39, No. 1, 2002.
5. Pinkerton, J.L., Moses, R. W., "A Feasibility Study to Control Airfoil Shape Using THUNDER," NASA Technical Memorandum 4767.
6. Strelec, Justin K., Lagoudas, Dimitris C., "Fabrication and Testing a Shape Memory Alloy Actuated Reconfigurable Wing," <http://smart.tamu.edu/publications/docs/Proceedings/SPIE2002/wing/SPIE%20wing%20experiments.pdf>.
7. McGowan, Anna-Maria R., Washburn, Anthony E., Horta, Locas G., Bryant, Robert G., Cox, David E., Soichi, Emilie J., Padula, Sharon L., and Holloway, Nancy M., "Recent Results from NASA's Morphing Project," SPIE Paper No. 4698-11, presented at the 9<sup>th</sup> Annual International Symposium on Smart Structures and Materials, March 17-21, 2002, San Diego, California.
8. Simpson, J.O., Wise, S.A., Bryant, R.G., Cano, R.J., Gates, T.S., Hinkley, J.A., Rogowski, R.S., and Whitley, K.S., "Innovative Materials for Aircraft Morphing," Materials Division, NASA Langley Research Center.

9. Saggere, Laxminarayana, Kota, Sridhar, "Static Shape Control of Smart Structures Using Compliant Mechanisms," AIAA Journal, Vol. 37, No. 5, May 1999.
10. Jacob, J.D., "On the Fluid Dynamics of Adaptive Airfoils," Proceedings of 1998 ASME International Mechanical Engineering Congress and Exposition, November 15-20, 1998, Anaheim, CA, USA.
11. Benson, Tom, "Wright Brothers' Wing Warping," NASA Glenn Research Center, <http://wright.nasa.gov/airplane/warp.html>, September 26, 2003.
12. Parker, H.F., "The Parker Variable Camber Wing," Report No. 77, Annual Report National Advisory Committee for Aeronautics, 1920.
13. Parks, Dennis, "Daniel Guggenheim International Safe Airplane Competition," Vintage Literature, [http://www.aircrash.org/burnelli/ch\\_a\\_gx3a.htm](http://www.aircrash.org/burnelli/ch_a_gx3a.htm).
14. U.S. Centennial of Flight Commission, "Slotted Wing, Flaps, and High Lift Devices," [http://www.centennialofflight.gov/essay/Evolution\\_of\\_Technology/High\\_Lift\\_Devices/Tech6.htm](http://www.centennialofflight.gov/essay/Evolution_of_Technology/High_Lift_Devices/Tech6.htm).
15. Van Dam, C.P., "The Aerodynamic Design of Multi-Element High-Lift Systems for Transport Airplanes," Progress in Aerospace Sciences, Vol. 38, pp. 101-144, 2002.
16. "High-Lift Aerodynamics," Advanced Topics in Aerodynamics, [http://aerodyn.org/HighLift/high\\_lift.html](http://aerodyn.org/HighLift/high_lift.html).
17. "High Lift Systems: Introduction", <http://adg.stanford.edu/aa241/highlift/highliftintro.html>.
18. Mason, W.H., "High-Lift Aerodynamics," [http://www.aoe.vt.edu/~mason/Mason\\_f/ConfigAeroHiLift.pdf](http://www.aoe.vt.edu/~mason/Mason_f/ConfigAeroHiLift.pdf).
19. Powers, S. G., Webb, L.D., Friend, E.L., Lokos, W.A., "Flight Test Results from a Supercritical Mission Adaptive Wing with Smooth Variable Camber," NASA Technical Memorandum 4415, 1992.
20. AFTI-111 Photo Gallery Contact Sheet, <http://www.dfrc.nasa.gov/Gallery/Photo/F-111AFTI/HTML/>.
21. Pendleton, E, Griffin, K.E., Kehoe, M.W., Perry, B, "A Flight Research Program for Active Aeroelastic Wing Technology," AIAA-96-1574.
22. Perry, Boyd III, Cole, Stanley R., "Summary of an Active Flexible Wing Program," Journal of Aircraft, Vol. 32, No.1, January-February 1995, pp. 10-15.

23. Zink, P.S., Mavris, D. N., Flick, P. M., Love, M. H., “Impact of Active Aeroelastic Wing Technology on Wing Geometry Using Response Surface Methodology,” CEAS/ AIAA/ICASE/NASA Langley International Forum on Aeroelasticity and structural Dynamics, Williamsburg, VA, June 22-25, 1999.
24. Zink, P.S., Marvis, D. N., Raveh, D. E., “Integrated Structural/Trim Optimization for Active Aeroelastic Wing Technology,” AIAA 2000-4827.
25. Barr, Larine, “Wing-Warping Aircraft Has Debut Flight,” [News@afri](mailto:News@afri), Vol. III, Issue 11, November 2002.
26. Buttrill, C.S., Bacan, B.J., Heeg, J., Houck, J.A., and Wood, D.V., “Aeroservoelastic Simulation of an Active Flexible Wing Wind Tunnel Model,” NASA Technical Paper 3510.
27. Gano, Shawn E., Renaud, John E., “Optimized Unmanned Aerial Vehicle with Wing Morphing for Extended Range and Endurance,” AIAA 2002-5668.
28. Gano, Shawn, Renaud, John E., “Shape Optimization for Conforming Airfoil Cross-Sections,” 44<sup>th</sup> AIAA/ASME/ASCE/AHS Structures, Structural Dynamics, and Materials Conference, Norfolk, VA, 7-10 April 2003.
29. Kudva, J., Appa, K., Martin, C.A., Jardine, A.P., Sendekyj, G., Harris, T., McGowan, A., and Lake, R., “Design, Fabrication, and Testing of the DAPRA/Wright Lab “Smart Wing” Wind Tunnel Model,” AIAA Paper 97-1198, April 1997.
30. Schere, L.B., Martin, C.A., West, M., Florance, J.P., Wieseman, C.D., Burner, A.W., and Fleming, G.A., “DARPA/AFRL/NASA Smart Wing Second Wind Tunnel Test Results,” Proceedings of SPIE, Vol. 3674, July 1999, pp. 249-259.
31. Wall, Robert, “DARPA Eyes Materials for ‘Morphing’ Aircraft,” Next Century of Flight: Aviation Week’s AviationNow.com, [http://www.aviationnow.com/content/ncof/ncf\\_n66.htm](http://www.aviationnow.com/content/ncof/ncf_n66.htm), April 8, 2002.
32. Natarajan, A., Sulaeman, E., Pettit, G., Gern, F.H., Kapania, R.K., Robertshaw, H.H., Inman, D.J., “Inverse Approach in Smart Aeroelastic UCAV Wing Design,” [http://www.aoe.vt.edu/research/groups/mad/MAD\\_Meeting\\_2000/Presentations/ucav2000.pdf](http://www.aoe.vt.edu/research/groups/mad/MAD_Meeting_2000/Presentations/ucav2000.pdf).
33. Prock, Brian C., Weisshaar, Terrence A., Crossley William A., “Morphing Airfoil Shape Change Optimization with Minimum Actuator Energy as an Objective,” AIAA 2002-5401.

34. Naval Research Laboratory (James P. Thomas), "Structural Performance with Energy Storage for Air Vehicles Through Multifunctional Design and Fabrication," <http://mstd.nrl.navy.mil/6350/MfM.html>, April 18, 2003.
35. McMaster-Carr Catalog Page 884, <http://www.mcmaster.com>.
36. McMaster-Carr Catalog Page 873, <http://www.mcmaster.com>.
37. Bowman, Jason, Sanders, Brian, Weisshaar, Terrence, "Evaluating the Impact Morphing Technologies on Aircraft Performance," AIAA 2002-1631.
38. Anderson, John D., Jr., *Aircraft Performance and Design*, McGraw-Hill, New York, 1999.
39. Anderson, John D., Jr., *Introduction to Flight*, 3<sup>rd</sup> ed., McGraw-Hill, New York, 1989.
40. Abbott, Ira H. and Deonhoff, Albert E. Von, *Theory of Wing Sections*, Dover Publications, Inc., New York, 1959.
41. Drela, Mark, and Youngren Harold, "XFOIL 6.94 User Guide," 10 Dec 2001.
42. Bolonkin, Alexander, Gilyard, Glenn, B., "Estimated Benefits of Variable-Geometry Wing Camber Control for Transport Aircraft," NASA/TM-1999-206586, October 1999.
43. Air Force Flight Dynamics Laboratory, Flight Control Division, *USAF Stability and Control DATCOM*, Vol. 3, Section 6, Wright-Patterson Air Force Base, Ohio, October 1960, revised April 1978.
44. Raymer, Daniel P., *Aircraft Design: A Conceptual Approach*, 3<sup>rd</sup> ed., AIAA, Reston, VA, 1999.
45. Jacobs, E.N., Ward, K.E., and Pinkerton, R.M., "The Characteristics of 78 Related Airfoil Sections From Tests in the Variable-density Wind Tunnel," NACA report No. 460.
46. Gerritsma, M.I., and Van Oudheusden, B.W., "Aerodynamics B, AE2-115 I," [http://www.aero.lr.tudelft.nl/~bvo/aerob/aero-B\\_ch4.ppt](http://www.aero.lr.tudelft.nl/~bvo/aerob/aero-B_ch4.ppt).